

Sensitivity of Multiangle Imaging to Aerosol Optical Depth, and to Pure-Particle Size Distribution and Composition Over Ocean

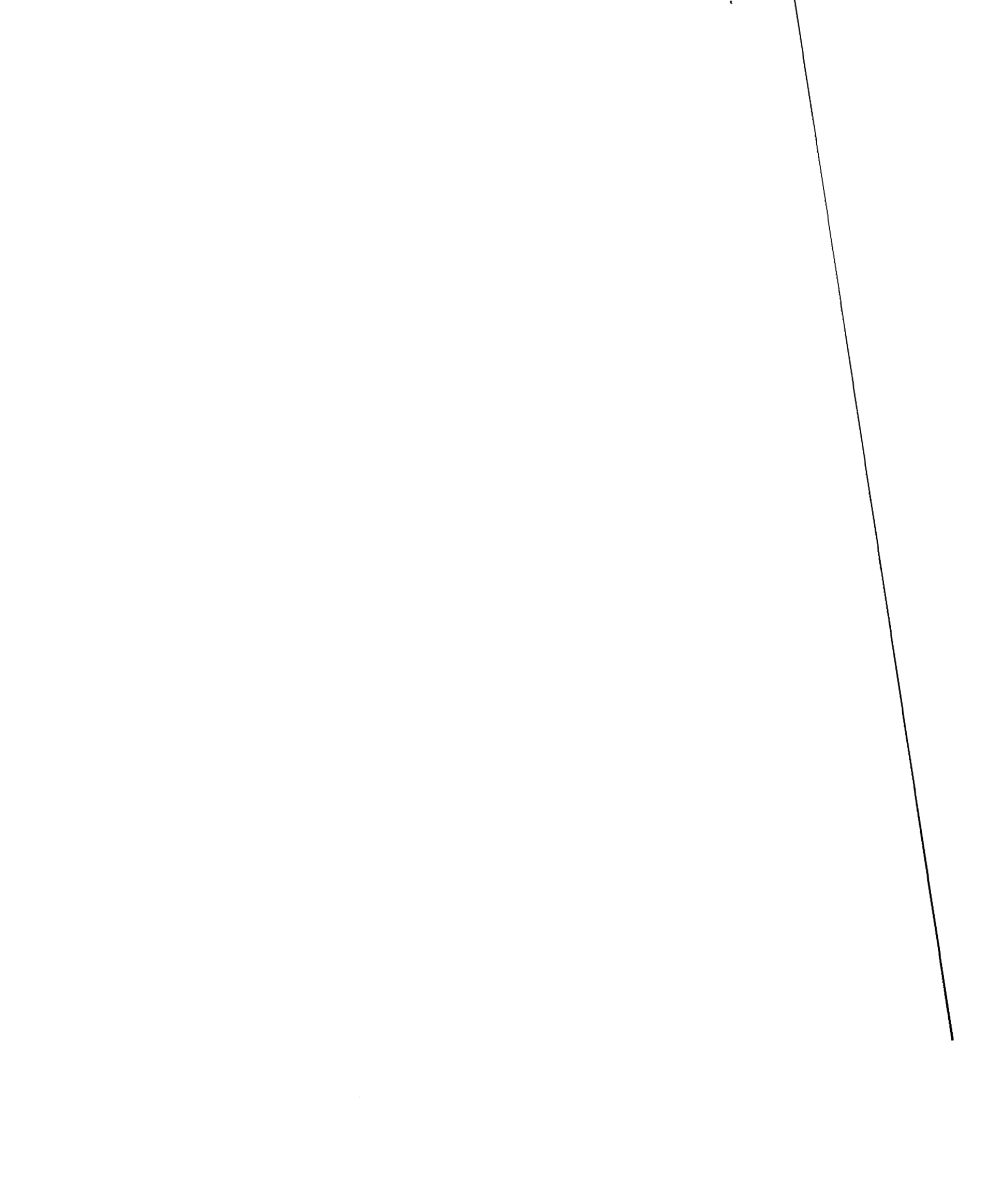
Ralph Kahn, Pranab Banerjee, Duncan McDonald, and David J. Diner

Jet Propulsion Laboratory, California Institute of Technology

4800 Oak Grove Drive, Pasadena CA 91109

Submitted to: The Journal of Geophysical Research, Atmospheres
 EOS-AM1 Special Issue

December 4, 1997



Abstract

Multiangle, multispectral remote sensing observations, such as those anticipated from the Earth Observing System (EOS) Multi-angle Imaging SpectroRadiometer (MISR), can significantly improve our ability to constrain aerosol properties from space. Simulations over cloud-free, calm ocean conditions were studied, for pure particles with natural ranges of optical depth, particle size, and indices of refraction. According to the theoretical simulations, we can retrieve column optical depth from measurements over calm ocean, for all but the darkest particles, with typical size distributions and compositions, to an accuracy of at least 0.05 or 10%, whichever is larger, even if the particle properties are poorly known. Over a dark ocean, constraints on the optical depth of one common particle type, soot, are very poor if the soot opacity is greater than about a tenth. The simulated measurements also allow us to distinguish spherical from non-spherical particles, to separate two to four compositional groups based on indices of refraction, and to identify three to four distinct size groups between 0.1 and 2.0 microns characteristic radius at most latitudes. Most of the information about particle microphysical properties comes in the “accumulation mode” sizes, where particles transition from Rayleigh to large-particle scattering regimes for the MISR wavelengths.

Based on these results, we expect to distinguish air masses containing different aerosol types, routinely and globally, with multiangle remote sensing data. Such data complements in situ and field data, which can provide detailed information about aerosol size and composition. An extension of this study to mixtures of pure particles is part of continuing work.

1. Introduction

Recent advances in modeling the Earth’s climate have brought us to a point where the contributions made by aerosols to the global radiation budget have an impact on the results (e.g., *Andreae*, 1995; *Charlson et al.*, 1992; *Hansen et al.*, 1997; *Penner et al.*, 1994). Aerosols are thought to contribute significantly to direct radiative forcing in the atmosphere, and indirectly, through their influence as nucleation sites for cloud particles. Knowledge of both aerosol optical depth and the microphysical properties of particles is needed to adequately model aerosol effects.

Currently, we must rely on satellite remote sensing to provide the spatial and temporal coverage required for global monitoring of atmospheric aerosols. However, the retrieval of aerosol properties by remote sensing is a notoriously under-determined problem. And the only operational, global-scale, satellite-based retrieval of aerosols derives aerosol optical depth from

single-angle, monospectral data, using assumed values for all the aerosol microphysical properties [Rao *et al.*, 1989; Stowe *et al.*, 1997].

Multiangle, multispectral remote sensing observations, such as those anticipated from the Earth Observing System (EOS) Multiangle Imaging SpectroRadiometer (MISR), provide a type of information about the characteristics of aerosols never before obtained from satellites [Diner *et al.*, 1991; 1997]. We plan to retrieve aerosol optical depth and aerosol "type," which represents a combination of index of refraction, size distribution, and shape constraints, globally, at 17.6 km spatial resolution.

MISR is scheduled for launch into polar orbit on the EOS-AM1 platform in June 1998. It will measure the upwelling visible radiance from Earth in 4 spectral bands centered at 446, 558, 672, and 866 nm, at each of 9 view angles spread out in the forward and aft directions along the flight path at 70.5°, 60.0°, 45.6°, 26.1°, and nadir. The maximum spatial sampling rate is 275 meters in the cross-track and along-track directions, at all angles except nadir, where the cross-track value is 250 meters. Over a period of 7 minutes, a 360 km wide swath of Earth comes into the view of the cameras at each of the 9 emission angles, providing a wide range of scattering angle coverage for each surface location. The data will be used to characterize aerosol optical depth, aerosol type, surface albedo and bi-directional reflectance, and cloud properties. Complete coverage of latitude bands will take 9 days at the equator and 2 days in polar regions; the nominal mission lifetime is 6 years.

This is the second in a series of papers that explores our ability to retrieve information about atmospheric aerosols from MISR. The first paper [Kahn *et al.*, 1997] asks how well we can distinguish spherical from non-spherical particles having microphysical properties commonly associated with mineral dust from the Sahara desert. Based on theoretical simulations, we show that over calm ocean surfaces, and with expected ranges of particle optical depth and size distribution, MISR can distinguish spherical from non-spherical particles, and can retrieve column optical depth for these non-spherical particles to an accuracy of at least 0.05 or 10%, whichever is larger. At most latitudes, MISR can also identify three to four distinct size groups between 0.1 and 2.0 microns characteristic radius.

In the current paper, we expand this work to include natural ranges of optical depth, particle size distribution, and composition for common types of spherical particles. We concentrate on situations under which the MISR sensitivity to particle properties (except possible absorption) is likely to be greatest: over calm ocean. These results provide a theoretical upper bound on the

sensitivity of actual MISR retrievals for all aerosol properties except particle single scattering albedo, which may be better constrained over land surfaces with spatially varying contrast.

For this study, we consider atmospheres containing “pure” particle types -- aerosol populations with uniform composition, and with aerosol sizes characterized by unimodal, log-normal distribution functions. A subsequent paper will treat the MISR sensitivity to mixtures of particle types.

2. Our Approach to the Aerosol Sensitivity Study

Our overall approach is to designate one set of simulated reflectances as MISR “measurements,” with an atmosphere having fixed aerosol optical depth (τ_a), particle characteristic radius (r_a), real index of refraction (nr_a), and imaginary index of refraction (ni_a). We then test whether they can be distinguished, within instrument uncertainty, from a series of “comparison” model reflectances. For the comparison models, we systematically vary the four comparison model parameters: aerosol optical depth (τ_c), characteristic radius (r_c), real index of refraction (nr_c), and imaginary index of refraction (ni_c). The goal is to determine the ranges of comparison model properties that give an acceptable match with the measurements.

Prior to launch of the MISR instrument, we rely on simulations of top-of-atmosphere radiation to explore the sensitivity of multiangle observations to aerosol properties. The MISR Team has developed a radiative transfer code, based on the adding-doubling method [Hansen and Travis, 1974], to simulate reflectances as would be observed by MISR, for arbitrary choice of aerosol type and amount, and variable surface reflectance properties [Diner *et al.*, 1997]. For the present study we simulated MISR measurements over a Fresnel-reflecting calm ocean surface, in a cloud-free, Rayleigh scattering atmosphere with a surface pressure of 1.013 bar and a standard midlatitude temperature profile. (In the actual MISR retrievals over ocean, we include sun glint and whitecap models that depend on near-surface wind speed [Martonchik *et al.*, 1997].)

A layer containing particles with selected optical depth, spectral single scattering albedo, extinction coefficient, and single scattering phase function is placed between the gas component and the surface. Extinction and scattering properties for log-normal distributions of spherical particles are derived at selected values of particle characteristic radius (r_c), real index of refraction, and imaginary index of refraction, using a standard Mie scattering code. The log-normal function is given as:

$$lgnrm(r) = \frac{1}{r \ln(\sigma) \sqrt{2\pi}} \exp \left[-\frac{(\ln(r) - \ln(r_c))^2}{2 (\ln(\sigma))^2} \right] \quad (1)$$

The width parameter (σ) in this function is set to 2.5 for accumulation, 2.0 for coarse, and 2.0 for nucleation modes, representing fairly broad, natural distributions of particles.

2.1. Testing the Agreement Between Comparison Models and “Measurements”

Over ocean, the MISR retrieval makes use of up to 18 measurements: 9 angles at each of the 2 longest MISR wavelengths (Bands 3 and 4, centered at 672 and 866 nm, respectively), where the water surface is darkest. We define 4 test variables to decide whether a comparison model is consistent with the measurements. Each is based on the χ^2 statistical formalism [e.g., *Bevington and Robinson, 1992*].

One test variable weights the contributions from each observed reflectance according to the slant path through the atmosphere of the observation:

$$\chi_{abs}^2 = \frac{1}{N \langle w_k \rangle} \sum_{l=3}^4 \sum_{k=1}^9 \frac{w_k \left[\rho_{meas}(l,k) - \rho_{comp}(l,k) \right]^2}{\sigma_{abs}^2(l,k)} \quad (2)$$

where ρ_{meas} is the simulated “measurement” of atmospheric equivalent reflectance and ρ_{comp} is the simulated equivalent reflectance for the comparison model. (We define equivalent reflectance as the radiance multiplied by π , and divided by the exo-atmospheric solar irradiance at normal incidence.) l and k are the indices for wavelength band and camera, N is the number of measurements included in the calculation, w_k are weights, chosen to be the inverse of the cosine of the emission angle appropriate to each camera k , $\langle w_k \rangle$ is the average of weights for all the measurements included in the summation. σ_{abs} is the absolute calibration uncertainty in the equivalent reflectance for MISR band l and camera k . For MISR, the nominal value of σ_{abs}/ρ falls between 0.03 for a target with equivalent reflectance of 100%, and 0.06 for an equivalent reflectance of 5%, in all channels [*Diner et al., 1997*]. For the simulations, we model σ_{abs} as varying linearly with equivalent reflectance (Figure 1).

χ^2_{abs} alone reduces 18 measurements to a single statistic. χ^2_{abs} emphasizes the absolute reflectance, which depends heavily on aerosol optical depth for bright aerosols over a dark surface. However, there is more information in the measurements that can improve the retrieval discrimination ability.

A second χ^2 test variable emphasizes the geometric properties of the scattering, which depend heavily on particle size and shape. This test variable takes advantage of the smaller camera-to-camera relative uncertainty as compared to the absolute uncertainty -- each spectral measurement is divided by the corresponding spectral measurement in the nadir camera:

$$\chi^2_{geom} = \frac{1}{N \langle w_k \rangle} \sum_{l=3}^4 \sum_{\substack{k=1 \\ k \neq nadir}}^9 w_k \left[\frac{\rho_{meas}(l,k)}{\rho_{meas}(l,nadir)} - \frac{\rho_{comp}(l,k)}{\rho_{comp}(l,nadir)} \right]^2 \frac{1}{\sigma^2_{geom}(l,k)} \quad (3a)$$

Here σ^2_{geom} (a dimensionless quantity) is the uncertainty in the camera-to-camera equivalent reflectance ratio, derived from the expansion of errors for a ratio of measurements ($\sigma^2(f(x,y)) = (df/dx)^2 \sigma_x^2 + (df/dy)^2 \sigma_y^2$ [e.g., *Bevington*, 1969]):

$$\sigma^2_{geom}(l,k) = \frac{\sigma^2_{cam}(l,k)}{\rho^2_{meas}(l,nadir)} + \frac{\sigma^2_{cam}(l,nadir) \rho^2_{meas}(l,k)}{\rho^4_{meas}(l,nadir)} \quad (3b)$$

$\sigma_{cam}(l,k)$ is the contribution of (band l , camera k .) to the camera-to-camera relative calibration reflectance uncertainty. σ_{cam} is nominally one third the corresponding value of σ_{abs} for the MISR instrument [*Diner et al.*, 1997]. Note that σ_{cam} includes the effects of systematic calibration errors for ratios of equivalent reflectance between cameras, as well as random error due to instrument noise, though the latter has been neglected in these simulations, based on the high signal-to-noise ratio demonstrated during MISR camera testing [*Bruegge et al.*, 1997].

Similarly, we define a spectral χ^2 as:

$$\chi_{spec}^2 = \frac{1}{N \langle w_k \rangle} \sum_{k=1}^9 \frac{w_k \left[\frac{\rho_{meas}(band\ 4,k)}{\rho_{meas}(band\ 3,k)} - \frac{\rho_{comp}(band\ 4,k)}{\rho_{comp}(band\ 3,k)} \right]^2}{\sigma_{spec}^2(l,k)} \quad (4a)$$

with:

$$\sigma_{spec}^2(l,k) = \frac{\sigma_{band}^2(l,k)}{\rho_{meas}^2(band\ 3,k)} + \frac{\sigma_{band}^2(band\ 3,k) \rho_{meas}^2(l,k)}{\rho_{meas}^4(band\ 3,k)} \quad (4b)$$

$\sigma_{band}(l,k)$ is the contribution of (band l , camera k) to the band-to-band relative calibration reflectance uncertainty. σ_{band} is nominally one third the corresponding value of σ_{abs} for the MISR instrument.

We include a maximum deviation test variable that is the single largest term contributing to χ_{abs}^2 (see equation (2)):

$$\chi_{max\ dev}^2 = \underset{l,k}{Max} \frac{\left[\rho_{meas}(l,k) - \rho_{comp}(l,k) \right]^2}{\sigma_{abs}^2(l,k)} \quad (5)$$

All the other test variables are averages of up to 18 measurements. $\chi_{max\ dev}^2$ makes greatest use of any band-specific or scattering-angle-specific phenomenon, such as a rainbow or a spectral absorption feature, in discriminating between the measurements and comparison models.

2.2. Evaluating The χ^2 Test Variables

Since each χ^2 variable is normalized to the number of channels used, they are “reduced” χ^2 quantities, and a value less than or about unity implies that the comparison model is indistinguishable from the measurements. Values larger than about 1 imply that the comparison model is not likely to be consistent with the observations. In more detail, $\chi^2 < 1$ means that the

average difference between the measured and comparison quantities is less than the associated measurement error. If the quantity in the numerator of a reduced χ^2 variable definition with 17 degrees of freedom is sampled from a population of random variables, an upper bound of 1 corresponds formally to an average confidence of about 50% that we are not rejecting a comparison model when in fact it should be accepted; for an upper bound of 2, that confidence increases to almost 99% [Bevington and Robinson, 1992]. (This is not strictly true for the “ χ^2 ” variables defined here. They are actually the averages of correlated measurements from multiple bands and cameras, so a given upper bound is likely to be a less stringent constraint. Each term contributing to these variables may itself be distributed as χ^2 .)

To illustrate the values of the test variables, we developed a color bar with 3 segments: a logarithmic segment for values between 10^{-5} and 1 depicted in shades of blue, a logarithmic segment for values between 5 and 10^4 depicted in shades of red, and a linear segment shown in light green, yellow, and orange shades for the intermediate values. Thus, red shades in the figures indicate situations where the model is clearly distinguishable from the measurement, whereas blue shades indicate that the model is indistinguishable from the measurement. Black is reserved for exact agreement between model and measurement, which can occur in this study because we are working with simulated observations. Note that the color table has been designed so that if these figures are photocopied in black and white, first-order information about the ability to distinguish among models is preserved.

2.3. Organizing the Study of the 8-Dimensional Space

There are 4 independent variables associated with aerosols from the “atmosphere” (τ_a , r_a , nr_a , and ni_a) and another 4 representing the same aerosol properties for the comparison models (τ_c , r_c , nr_c , and ni_c). We have defined 4 dependent variables to be used in comparing the measurements with the models (χ^2_{abs} , χ^2_{geom} , χ^2_{spec} , and χ^2_{maxdev}). This creates an 8-dimensional space, with 4 scalar elements at each point in the domain.

Based on climatological data, we select natural ranges of aerosol optical depth, particle size distribution characteristic radius, and indices of refraction to study. Simulations are run for a grid of values in these 4 variables. We systematically explore the properties of this space by selecting a

subset of these values as the “atmosphere” cases, and calculating all 4 test variables that compare each of the “atmosphere” cases with all the cases in the grid.

We built an interactive system that plots χ^2 values for any 3 independent variables. We can slice through this volume and display the color-bar values of any of the test variables, or for the maximum of the 4 test variables, in a 2-dimensional plot. For each point in these plots, we can call up the values of all the independent and dependent variables, as well as the calculated reflectance values for the associated atmosphere and comparison model. We also created a summary tool that searches numerically through the space, identifies the minimum and maximum values of any of the independent variables that meet user-specified criteria on the test variables, and displays the results as bar charts. These tools are illustrated in the next section. With them, we create general summaries of the retrieval sensitivity, and can identify the specific equivalent reflectances that contribute to these results.

3. Sensitivity to Aerosol Optical Depth, Characteristic Radius, and Indices of Refraction

To capture in a sensitivity study the range of likely aerosol effects, we systematically explore the properties of 3 parameter spaces. They cover natural ranges of aerosol optical depth, particle size distribution characteristic radius, and indices of refraction for “nucleation,” “accumulation,” and “coarse” mode particles. Table 1 lists the ranges for all 3 parameter spaces. Simulations were run on a grid of linearly spaced values in all dimensions except the imaginary index of refraction, for which the grid spacing is logarithmic.

We concentrate on the “accumulation” mode particles because they are expected to contribute most to total aerosol optical depth at visible wavelengths. Nucleation mode particles are much less efficient at extinguishing light, and coarse mode particles are usually rare. However, even for the accumulation mode size range, not all locations within the parameter space are likely to be filled by commonly occurring atmospheric aerosols. The properties of common aerosol types are summarized in Table 2. There are 5 basic compositions -- sulfates, mineral dust, sea salt, biomass burning particles, and soot. Sizes range from tiny soot particles to coarse mineral dust and sea salt. With the exception of soot, particles have low imaginary index of refraction and high single scattering albedo in the red and near-infrared channels. The MISR aerosol retrievals use this climatology to help constrain the results in the operational MISR retrieval [Martonchik *et al.*, 1997]. We also use the climatology as a guide to interpreting the results of the sensitivity calculations. (The present study deals with spherical particles. In the MISR retrievals, and in our previous sensitivity study (Kahn *et al.*, 1997), mineral dust particles are treated as non-spherical.)

3.1. Constraints on Aerosol Optical Depth

We begin with the question: Given MISR data over a cloud-free, dark ocean surface, how well can we constrain the optical depth (τ_a) of atmospheric aerosols?

Figure 2 is an example of a comparison matrix, taken from within the accumulation mode parameter space. In this figure, the atmospheric particles have fixed microphysical properties typical of sulfate particles in the troposphere (e.g., *Shettle and Fenn*, 1979): dry values of $nr_a = 1.53$, $ni_a = 0.0$, and log-normal size distribution with $r_a = 0.5$ microns and width of 1.86. The particles are hydrated to equilibrium at 70% relative humidity, using the model of *Hanel* (1976).

There are 4 panels in Figure 2. Each contains all the test results for one choice of atmospheric optical depth, so within a panel, all the modeled properties of the atmospheric aerosols are fixed. The 4 panels correspond to atmospheric aerosol optical depths at 0.55 microns wavelength of 0.05, 0.1, 0.5, and 1.0, respectively.

The optical depths of the comparison models at 0.55 microns vary systematically from 0.05 to 1.0 in increments of 0.05 across the bottom of each panel in Figure 2; the dry radii of the comparison models vary from 0.05 to 2.0 microns in increments of 0.05 along the vertical axis. Refractive indices for the comparison model are the same as those for the atmosphere in the slice shown here.

Each box within the panel is divided into 5 fields, 4 showing the colors corresponding to each of the χ^2 test variables, and the background, which is colored with the largest (most red) χ^2 value among the 4 tests. So the box for each comparison model tells whether that model can be distinguished from the atmosphere with MISR data, and which test(s) provide the most constraining information.

In Figure 2, the blue areas, which indicate comparison models indistinguishable from the atmosphere with MISR data, are small and vertically oriented -- there are acceptable comparison models with a broad range of r_c , but a narrow range of τ_c , on this scale. Close examination of the surrounding boxes shows that χ^2_{maxdev} and χ^2_{abs} are responsible for constraining τ_c so tightly. Both tests rely on the absolute brightness. This is expected, since the absolute scene brightness increases with optical depth for non-black particles over a black surface.

We have studied sensitivity to optical depth over the entire parameter spaces given in Table 1. The results for accumulation and coarse mode particles are summarized in Figures 3a and 3b, respectively. These bar charts show the sensitivity, as indicated by the range of acceptable comparison model optical depth, along the vertical axis, for all comparison models in the accumulation mode parameter space that give acceptable matches to an atmosphere with fixed particle properties. For these figures, an acceptable comparison model is one for which all four χ^2 test variables fall between 0 and 2. Each group of 4 bars corresponds to 4 choices of atmosphere particle optical depth (0.05, 0.1, 0.5, and 1.0 in MISR band 2), for fixed atmosphere particle radius. The groups are spread along the horizontal axis to indicate different choices of atmosphere particle radius. Each panel of Figure 3 represents a fixed value of atmosphere particle imaginary index of refraction. The real index of refraction for atmosphere particles is fixed at 1.47 for all these charts, but within its natural range of values, this quantity has very little effect on these results. Comparison model properties: r_c , nr_c , and ni_c , are free to vary over the entire parameter space given in Table 1.

Sensitivity to optical depth is as low as 0.05, and remains within 10% regardless of the physical properties of the particles, as long as ni_a is 0.0. This covers all natural cases involving sulfate and sea salt particles (Table 2). The lower limit of 0.05 is set by the assumed camera calibration uncertainty, which reaches a limiting value for low reflectance levels (Figure 1). Calibration uncertainty affects the sensitivity through " σ " in the χ^2 test variable definitions. The choice of grid spacing for this study was made in consideration of this limit. During MISR operations, in-flight measured radiometric uncertainty for each camera will be used directly for calculating the χ^2 test variables in the retrievals [Bruegge *et al.*, 1997].

According to Figure 3, as ni_a increases, sensitivity to aerosol optical depth degrades and becomes more dependent on atmospheric aerosol optical depth, particle size, and imaginary refractive index. Sensitivity to τ_a also decreases as optical depth increases, particularly from 0.05 to 0.5. Part of the degradation comes from the increased contribution of multiple scattering to the signal as scene brightness increases. For example, when $r = 0.5$ microns, $nr = 1.47$, and $ni = 0.13$, the multiple scattering contribution to the steepest forward-looking MISR camera increases from about 20% of the signal to nearly half as τ increases from 0.1 to 0.5. As τ_a increases further, the sensitivity to optical depth increases again in some cases. Here the multiple scattering contribution is not growing as rapidly, whereas the total aerosol signal relative to background Rayleigh scattering continues to increase.

We now examine in detail the sensitivity of the multiangle retrieval to particles that have non-zero ni . When $ni = 0.0$, most of the information about optical depth comes from systematic increases in brightness as τ increases. As Figure 4 shows, when $ni > 0.0$, the single scattering phase functions in the back-scattering directions decrease with increasing radius. For a given set of measured radiances, we find agreement based on the χ^2 criteria for several comparison models, some with smaller radius and lower optical depth, others with larger radius and higher optical depth. This creates the higher uncertainty in τ_c found in Figure 3.

In terms of the MISR retrieval, we are most interested in aerosol types that are climatologically likely -- those with non-zero ni are biomass burning particles, mineral dust, and soot. In the red and near-infrared channels, ni for biomass burning particles in Table 2 is around 0.004. For all accumulation mode particles, and for optical depths less than 0.5, the range of optical depth for acceptable comparison models falls within 10% of the atmospheric value. This covers the expected natural range of conditions except near source regions, which are on land but may be close to a coast. If column optical depths of these particles reach 0.5, or if coarse sized biomass burning particles form, the sensitivity of MISR to optical depth will be diminished. [Note that the differences between the bars for $r_a = 2$ microns in corresponding charts of Figures 3a and 3b arise because the ranges of comparison model particle sizes for the two cases are different (Table 1).]

For mineral dust, ni in Table 2 for the red channel is also about 0.004, a value representative of the optically important dust component in many global studies (e.g., *Tegen and Lacis*, 1996). But a great variety of mineral dust particle types are known to occur in nature (*Sokolik and Toon*, 1996). With increasing ni_a or r_a , sensitivity to optical depth degrades. In the climatologically unlikely situation that optical depths of a few tenths or more of coarse mode dust are present, or ni_a exceeds 0.008, the retrieved optical depth will be uncertain to 20% or more. If no other information is available, MISR results will depend upon the assumptions we make about mineral dust properties, particularly regarding the imaginary index of refraction. [In the actual MISR retrievals, we use optical properties for mineral dust that take into account non-spherical shapes.]

The poorest sensitivity to optical depth occurs when dark particles (those having large ni) are found over the dark ocean surface. Soot particles fall into this category, but they are smaller than the other particle types in Table 2, and lie below the size ranges covered in Figure 3. Figure 5 covers this case, giving bar charts for part of the nucleation mode parameter space. It shows that even for tiny particles, multiangle data is not sensitive to the optical depth of very dark particles over a dark

surface. This is an inherent limitation of the technique. On the spatial scale of 17.6 km that applies to the MISR aerosol product, we expect that optical depths for pure soot will rarely exceed a few tenths over ocean. In addition, soot is most likely to appear mixed with other particle types having much lower ni . Our sensitivity to optical depth for such mixtures may be higher, and is the subject of continuing work.

Based on the results of this section, we expect the MISR aerosol optical depth retrieval sensitivity over ocean to fall within 0.05 or 10%, whichever is larger, for climatologically likely aerosol situations. However, the measurements are insensitive to optical depth for τ_a greater than about 0.1 of dark mineral or soot particles. We plan to use in situ measurements whenever possible to improve our assumptions about particle properties.

3.2. Constraints on Particle Characteristic Radius

We now ask the question: Given MISR data over a cloud-free, dark ocean surface, how well can we constrain the characteristic radius (r_a) of a monomodal distribution of atmospheric aerosols?

Figure 6a is a bar chart showing the ranges of r_c for all the comparison models in the accumulation mode parameter space that give acceptable matches to an atmosphere with fixed particle properties. Figure 6b is a similar set of charts for coarse mode sizes. In these charts, the real index of refraction for the atmosphere particles (nr_a) varies from column to column, and imaginary index of refraction (ni_a) varies from row to row. Comparison model properties: τ_c , nr_c , and ni_c , are free to vary over the entire parameter space given in Table 1. An acceptable match is a case for which all four χ^2 test variables fall between 0 and 2. Bars are produced for 8 choices of atmospheric particle radius (r_a) in each mode. For each r_a , bars are produced for 4 choices of atmosphere optical depth τ_a (0.05, 0.1, 0.5 and 1.0) in MISR band 2.

At each r_a , the range of acceptable r_c generally decreases as τ_a increases. This means we have better-constrained aerosol characteristic radius retrievals with increasing τ_a . We expect such behavior: by increasing the amount of aerosol, the contribution of aerosols to the measured radiance is increased, relative to the contribution from Rayleigh scattering gas. Some exceptions occur when increased instrument radiometric uncertainty, caused by the greater scene brightness (Figure 1), is enough to offset the increased aerosol signal.

Especially when τ_a is greater than 0.05, the constraint on r_c is tight for accumulation mode atmospheric particle distributions with characteristic radius smaller than about 0.8 microns. For larger particles, r_c is poorly constrained by simulated MISR data over ocean. This behavior is traced to the particle scattering phase function, which goes through a transition from “small” (Rayleigh) to “large” (geometric) regimes as particle size increases. At mid and high latitudes, the instrument samples scattering angles ranging from about 60° to 160° (Figure 7). Over this range of scattering angles, the particle single scattering phase functions change rapidly as r_a increases, until an upper limit is reached (Figure 8). For $ni = 0.0$, the transition occurs around $r_a = 0.8$ microns; for non-zero ni within the natural range, the transition occurs at r_a approaching 0.5 microns.

Based on Figure 6, MISR should be able to distinguish 3 to 4 groups of characteristic radius across the natural range of particle size, even if little is known a priori about composition, as long as the optical depth is greater than about 0.05. Most of this sensitivity occurs for particles with r_c between 0.1 and about 1 micron. The sensitivity to characteristic radius increases for higher optical depth and is greatest for particles with low imaginary index of refraction.

3.3. Constraints on Aerosol Composition

Figures 9 and 10 illustrate the sensitivity of MISR to real and imaginary indices of refraction, respectively. These parameters describe the composition of aerosols in our retrievals. As with particle size, sensitivity increases with atmospheric optical depth, and decreases for darker particles within the parameter space.

For $ni = 0$, our ability to constrain nr depends on τ_a and r_a . MISR sensitivity to index of refraction increases greatly for increasing τ_a . Sensitivity to nr is diminished for the smallest particles ($r_a = 0.1$), which fall in the Rayleigh scattering regime (Figure 8). nr discrimination is best for “medium” (accumulation mode) aerosols, and decreases for both small and large particles.

Overall, 1 to 2 groups of nr values can be distinguished over the natural range spanning $nr = 1.33$ to $nr = 1.55$, when τ_a is about 0.1. The number of groups increases to 2 to 3 nr values when τ_a is about 0.5, as long as the particles are not strongly absorbing. However, the data become insensitive to the real part of the index of refraction for darker particles (imaginary index larger than about 0.01).

Sensitivity to the imaginary part of the index of refraction itself follows a similar pattern, though the simulations suggest that when τ_a is 0.5 or greater, 3 to 4 groups of values between $ni = 0.0$ and about 0.5 can be distinguished. For optical depths of a few tenths, more typical of global ocean conditions, 1 or 2 groups of ni can be separated in the data.

3.4. Additional Considerations

The analysis presented in this paper is for midlatitude geometry. With the nominal orbit, the MISR instrument samples a broad range of scattering angles, between about 60° and 160° , in mid and high latitudes (Figure 7). The diminished range of scattering angles at low latitudes reduces the sensitivity of the retrieval to particle properties. Sensitivity to aerosol properties is also reduced by the presence of clouds, non-black surfaces due to whitecaps or plankton in the water, and sun glint. For sun glint, we eliminate the affected cameras from the retrieval, reducing the information content of the data, whereas we model whitecaps, which involves making assumptions about how they behave. All these phenomena are expected at some times and places in the MISR data. The goal of the present study is to explore the sensitivity of MISR to particle properties using simulated data, under the best observing conditions we anticipate. Once we receive actual measurements from the MISR instrument, we will assess the degree to which the quality of constraints on particle properties is reduced, under the range of conditions we encounter.

4. Conclusions

The enhanced ability of multiangle imaging to constrain aerosol properties, as compared to single-angle methods currently in operational use, comes from the known, varying geometric path through the atmosphere, and the range of scattering angles observed. Over ocean, MISR retrieval results are based on assumed surface reflectances, and assumptions that the atmosphere is cloud-free and the particles are horizontally homogeneous over the sampling region, which is 17.6 km at the surface, increasing to about 100 km at the tropopause, for the nominal instrument viewing geometry.

Based on our study of simulated data for pure particles, MISR retrievals over dark ocean will provide information about atmospheric aerosol optical depth, and some constraints on aerosol microphysical properties:

1. **Aerosol Optical Depth:** For non-absorbing particles, we expect to retrieve aerosol optical depth over calm ocean to 0.05 or 10%, whichever is larger, even if the particle properties are poorly known. As particle imaginary index of refraction increases, sensitivity to optical depth

degrades, and becomes dependent on particle size and optical depth. For optical depths less than 0.5, and for particle sizes and indices of refraction expected for all common particle types except soot (Table 2), optical depth sensitivity is still better than 10%. The measurements are less sensitive to optical depth for mineral dust and biomass burning particles with τ_a of 0.5 or greater, and are insensitive for τ_a greater than about 0.1 of soot particles.

2. **Aerosol Size Distribution:** We expect MISR to be able to distinguish 3 to 4 groups of characteristic radius across the natural range (“small,” “medium,” and “large”) over mid and high latitude ocean, even if little is known a priori about composition, as long as the aerosol optical depth is greater than about 0.05. Most of this sensitivity occurs for particles with r_c between 0.1 and about 1 micron, which covers the range of particle sizes where the scattering phase functions change from Rayleigh scattering behavior to curves with well-developed forward and back scattering peaks. The sensitivity to characteristic radius increases for higher optical depth, since there is more aerosol signal in these cases, and is greatest for less absorbing (low imaginary index of refraction) particles.

3. **Aerosol Composition:** MISR sensitivity to index of refraction increases strongly with increasing optical depth, and decreases with increasing ni . We can distinguish about 2 or 3 groups of real index of refraction values between 1.33 and 1.55, as long as the optical depth is 0.5 or larger and the particles are not strongly absorbing. Only 1 to 2 groups of nr values can be distinguished over the natural range when τ_a is about 0.1 or less. In addition, the data discriminate nr best for “medium” sized particles, and are insensitive to the real part of the index of refraction for dark particles. Sensitivity to the imaginary part of the index of refraction follows a similar pattern, though the simulations suggest that 3 to 4 groups of values for ni between 0.0 and about 0.5 can be distinguished, when τ_a is 0.5 or greater.

The actual sensitivity of MISR retrievals to particle properties over ocean will depend in part on the in-flight instrument calibration uncertainty, which sets the values of the σ 's, and governs our choice of the upper limit on χ^2 for accepting a comparison model as indistinguishable from the measurements. For this paper, we used pre-launch instrument specifications for calibration and noise levels. After launch, we will use the tools and the approach developed here to assess the in-flight sensitivity of MISR.

Our results suggest MISR will be able to distinguish "small," "medium," and "large" particle sizes, "dirty" or "clean" compositions, and "spherical" and "non-spherical" shapes, over the range of aerosol properties commonly found in nature. This should allow us to distinguish among the climatologically common particle types (Table 2), if each type occurs unmixed in the vertical column. We will use this improvement over simply assuming all the physical properties of particles, as is currently done for satellite aerosol monitoring, to identify air masses containing different aerosol types, as well as to provide more accurate retrievals of aerosol optical depth.

The strength of satellite retrievals is in their spatial and temporal coverage, which complements detailed composition and size distribution information obtained from in situ measurements. We plan to rely on ground-based and in situ instrument data to derive detailed compositions and size distributions of aerosols in air masses whenever possible.

This approach is similar to the way satellite-derived sea surface temperature (SST) data are often used -- the satellite data are assimilated with in situ measurements from ships and buoys. Satellite data provide a way to "interpolate" between field measurements, giving vastly more information about global, time-varying spatial distributions. With the help of additional constraints from in situ aerosol measurements, we plan to use the MISR data products for studies of global aerosol budgets.

In work currently underway, we are extending our pre-launch assessment of MISR sensitivity to deal with mixes of commonly occurring particles.

Acknowledgments. We thank our colleagues C. Bruegge and J. Martonchik for many discussions of these topics. This research is supported by the EOS-MISR instrument investigation, and by the Climate and Radiation Research and Analysis Program in the Earth Sciences Division of the National Aeronautics and Space Administration, under R. Curran. This work is performed at the Jet Propulsion Laboratory, California Institute of Technology, under contract with NASA.

References

Andreae, M.O., Climatic effects of changing atmospheric aerosol levels, in A. Henderson-Sellers, ed., *World Survey of Climatology, V.16: Future Climates of the World*, Elsevier, New York, 341-392, 1995.

Bevington, P.R. and D. K. Robinson, Data reduction and error analysis for the physical sciences, Second edition, McGraw-Hill, New York, pp. 328, 1992.

- Bruegge, C., N. Chrien, R. Kahn, J. Martonchik, and D. Diner, MISR radiometric uncertainty analyses and their utilization within geophysical retrievals, *IEEE Trans. Geosci. Remt. Sensing*, submitted, 1997.
- Charlson, R.J., S. Schwartz, J. Hales, R. Cess, J. Coakley, Jr., J. Hansen, and D. Hofmann, Climate forcing by anthropogenic aerosols, *Science* 255, 423-430, 1992.
- d'Almeida, G.A., P. Koepke, and E.P. Shettle, Atmospheric Aerosols: Global climatology and radiative characteristics, Deepak Publishing, 1991.
- Diner, D.J., C.J. Bruegge, J.V. Martonchik, G.W. Bothwell, E.D. Danielson, E.L. Floyd, V.G. Ford, L.E. Hovland, K.L. Jones, and M.L. White, A Multi-angle Imaging SpectroRadiometer for terrestrial remote sensing from the Earth Observing System, *Internat. J. Imaging Systems and Technol.* 3, 92-107, 1991.
- Diner, D.J., W. Abdou, T. Ackerman, K. Crean, H. Gordon, R. Kahn, J. Martonchik, S. McMuldroch, S. Paradise, B. Pinty, M. Verstraete, M. Wang, and R. West, MISR Level 2 Aerosol Retrieval Algorithm Theoretical Basis, JPL- D11400, Rev. C, 1997.
- Diner, D.J., J.C. Beckert, T.H. Reilly, C.J. Bruegge, J.E. Conel, R. Kahn, J.V. Martonchik, T.P. Ackerman, R. Davies, S.A.W. Gerstel, H.R. Gordon, J-P. Muller, R. Myneni, R.J. Sellers, B. Pinty, and M.M. Verstraete, Multiangle Imaging SpectroRadiometer (MISR) description and experiment overview, *IEEE Trans. Geosci. Remt. Sensing*, submitted, 1997.
- Hanel, G., The properties of atmospheric aerosol particles as functions of relative humidity at thermodynamic equilibrium with the surrounding moist air, *Adv. Geophys.* 19, 73-188, 1976.
- Hansen, J., M. Sato, A. Lacis, and R. Ruedy, The missing climate forcing, *Philos. Trans. R. Soc. London, Ser. B*, 352, 231-240, 1997.
- Hansen, J.E., and L.D. Travis, Light scattering in planetary atmospheres, *Space Sci. Rev.* 16, 527-610, 1974.
- Kahn, R., R. West, D. McDonald, B. Rheingans, and M.I. Mishchenko, Sensitivity of multiangle remote sensing observations to aerosol sphericity, *J. Geophys. Res.* 102, 16861-16870, 1997.
- Martonchik, J.V., D.J. Diner, R. Kahn, T.P. Ackerman, M.M. Verstraete, B. Pinty, and H.R. Gordon, Techniques for the retrieval of aerosol properties over land and ocean using multiangle data, *IEEE Trans. Geosci. Remt. Sensing*, submitted, 1997.
- Mishchenko, M.I., L. Travis, R. Kahn, and R. West, "Modeling phase functions for dust-like tropospheric aerosols using a shape mixture of randomly oriented polydisperse spheroids," *J. Geophys. Res.* 102, 16, 831-16, 847, 1997.
- Mishchenko, M.I., W.B. Rossow, A. Macke, and A.A. Lacis, "Sensitivity of cirrus cloud albedo, bidirectional reflectance and optical thickness retrieval accuracy to ice particle shape," *J. Geophys. Res.* 101, 16, 973-16, 985, 1996.
- Penner, J.E., R.J. Charlson, J.M. Hales, N.S. Laulainen, R. Leifer, T. Novakov, J. Ogren, L.F. Radke, S.E. Schwartz, and L. Travis, Quantifying and minimizing uncertainty of climate forcing by anthropogenic aerosols, *Bul. Am. Meteor. Soc.* 75, 375-400, 1994.
- Pruppacher, H.R., and J.D. Klett, Microphysics of Clouds and Precipitation, D. Reidel, pp.714, 1978.

Rao, C.R.N., L.L. Stowe, and E.P. McClain, Remote sensing of aerosols over the oceans using AVHRR data: Theory, practice and applications, *Int. J. Remote Sensing* 10, 743-749, 1989.

Remer, L.A., Y.J. Kaufman, B.N. Holben, A.M. Thompson, and D. McNamara, Biomass burning aerosol size distribution and modeled optical properties, *J. Geophys. Res.*, submitted, 1997.

Shettle, E.P., and R.W. Fenn, Models for the aerosols of the lower atmosphere and the effects of humidity variations on their optical properties, AFGL-TR-79-0214, Air Force Geophysics Laboratory, pp.94, 1979.

Sokolik, I.N., and O.B. Toon, Direct radiative forcing by anthropogenic airborne mineral aerosols, *Nature* 381, 681-683, 1996.

Stowe, L.L., A.M. Ignatov, and R.R. Singh, Development, validation, and potential enhancements to the second-generation operational aerosol product at the National Environmental Satellite, Data, and Information Service of the National Oceanic and Atmospheric Administration, *J. Geophys. Res.* 102, 16923-16934, 1997.

Tegen, I., and A.A. Lacis, Modeling of particle size distribution and its influence on the radiative properties of mineral dust aerosol, *J. Geophys. Res.* 101, 19237-19244, 1996.

Wang, P.-H., M.P. McCormick, T.J. Swissler, M.T. Osborn, W.H. Fuller, and G.K. Yue, Inference of stratospheric aerosol composition and size distribution from SAGE II satellite measurements, *J. Geophys. Res.* 94, 8435-8446, 1989.

World Climate Programme WCP-112. A Preliminary Cloudless Standard Atmosphere for Radiation Computation. IAMAP (International Association for Meteorology and Atmospheric Physics), Boulder, CO, pp.53, 1984.

Figure Captions

Figure 1. MISR absolute radiometric uncertainty assumed for this study, based on nominal instrument requirements [Diner *et al.*, 1994] and laboratory measurements [Bruegge *et al.*, 1997]. These curves are assumed to apply to all cameras. The relative band-to-band and camera-to-camera uncertainties are assumed to be one third of the absolute uncertainty. During MISR retrievals, in-flight measured radiometric uncertainty for each camera will be used directly for calculating the χ^2 test variables.

Figure 2. Example of a comparison matrix. This shows the results of tests between an atmosphere containing tropospheric sulfate-like particles, and comparison models with ranges of optical depth and characteristic radius. For this example, all particles have initial (dry) indices of refraction set to $nr = 1.53$, $ni = 0.0$, and are hydrated to equilibrium with 70% relative humidity following Hanel (1976). The 4 panels correspond to atmospheric aerosol optical depths of 0.05, 0.1, 0.5, and 1.0 at 0.55 microns wavelength. In blue and black areas, the largest value for any test variable is less than 1, indicating that the comparison models that are indistinguishable from the simulated MISR data. Red areas indicate comparison models that are not consistent with the MISR observations. The calculations presented here and elsewhere in this paper are for midlatitude cases: the cosine of the solar zenith angle (μ_0) is 0.6, and the angle between the azimuth of the sun and the instrument viewing plane ($\Delta\phi$) is 26.0° .

Figure 3a. Bar chart showing the ranges of aerosol optical depth values (τ_a) for comparison models that give acceptable matches to an atmosphere with accumulation mode particles having real index of refraction $nr_a = 1.47$, imaginary index of refraction ni_a ranging from 0.0 to 0.50. For an acceptable match, all four χ^2 test variables must fall between 0 and 2. Bars are produced for 8 choices of atmospheric particle characteristic radius (r_a) between 0.1 and 2, arrayed along the horizontal axes. For each r_a , a group of 4 bars is produced, corresponding to 4 choices of atmospheric optical depth (τ_a). As shading increases, the bars represent values of τ_a increasing from 0.05 to 0.1, 0.5, and 1.0.

Figure 3b. Same as 3a, but for part of the coarse mode particle parameter space.

Figure 4. Particle scattering phase functions at the effective wavelength of the MISR near-infrared band for single-sized spherical particles in the coarse mode range, between 2.0 and 4.5

microns radius, and $nr = 1.47$. Three groups of phase functions are plotted, one with $ni = 0.0$, one with $ni = 0.004$, and one with $ni = 0.032$. These three groups correspond to the uppermost, middle, and lowest four lines, respectively, when viewed at scattering angles between 150° and 180° , the region where much of the MISR optical depth discrimination is made.

Figure 5. Bar chart showing the ranges of aerosol optical depth values (τ_c) for comparison models that give acceptable matches to atmosphere particles covering part of the nucleation mode parameter space that includes expected soot particle sizes and indices of refraction. Atmosphere particle characteristic radius is fixed at 0.01 microns. The imaginary index of refraction ni_a ranges from 0.0 to 0.50. For an acceptable match, all 4 χ^2 test variables must fall between 0 and 2. Bars are produced for 4 choices of real index of refraction (nr_a) between 1.33 and 1.55, arrayed along the horizontal axes. For each nr_a , a group of 4 bars is produced, corresponding to 4 choices of atmospheric optical depth (τ_a). As shading increases, the bars represent values of τ_a increasing from 0.025 to 0.05, 0.25, and 0.5.

Figure 6a. Bar chart showing the ranges of particle radius (r_c) for comparison models that give acceptable matches to an atmosphere with accumulation mode particles having selected values of real and imaginary indices of refraction. For an acceptable match, all four χ^2 test variables must fall between 0 and 2. Bars are produced for 8 choices of atmospheric particle radius (r_a). For each r_a , a group of 4 bars is produced, corresponding to 4 choices of atmospheric optical depth τ_a . As shading increases, the bars represent values of τ_a increasing from 0.05 to 0.1, 0.5, and 1.0.

Figure 6b. Same as 6a, but for part of the coarse mode particle parameter space.

Figure 7. Typical ranges of scattering angles covered by the 9 MISR cameras, in the nominal EOS-AM1 orbit, at high, middle, and low latitudes.

Figure 8. Particle scattering phase functions at the effective wavelength of the MISR near-infrared band for single-sized spherical particles with $nr = 1.47$, $ni = 0.0$, and radii ranging from 0.1 to 1.50 microns. This range covers the transition from small particle (Rayleigh) scattering to large particle scattering.

Figure 9a. Bar chart showing the ranges of particle real index of refraction (nr_c) for comparison models that give acceptable matches to an atmosphere with accumulation mode particles having

selected values of characteristic radius and imaginary index of refraction. For an acceptable match, all four χ^2 test variables must fall between 0 and 2. Bars are produced for 4 choices of atmospheric particle real index of refraction (nr_a). For each nr_a , a group of 4 bars is produced, corresponding to 4 choices of atmospheric optical depth (τ_a). As shading increases, the bars represent values of τ_a increasing from 0.05 to 0.1, 0.5, and 1.0.

Figure 9b. Same as 9a, but for part of the coarse mode particle parameter space.

Figure 10a. Bar chart showing the ranges of particle imaginary index of refraction (ni_c) for comparison models that give acceptable matches to an atmosphere with accumulation mode particles having selected values of characteristic radius and real index of refraction. For an acceptable match, all four χ^2 test variables must fall between 0 and 2. Bars are produced for 4 choices of atmospheric particle imaginary index of refraction (ni_a). For each ni_a , a group of 4 bars is produced, corresponding to 4 choices of atmospheric optical depth (τ_a). As shading increases, the bars represent values of τ_a increasing from 0.05 to 0.1, 0.5, and 1.0.

Figure 10b. Same as 10a, but for part of the coarse mode particle parameter space.

Table 1. The Parameter Space of Aerosol Properties Used in this Study

| | Minimum Value | Maximum Value | # Divisions |
|---|--------------------------|--------------------------|------------------------|
| Aerosol optical depth at 0.55 microns* | 0.05 | 1.00 | 20 |
| Real Index of Refraction | 1.33 | 1.55 | 12 |
| Imaginary Index of Refraction | 0.0 | 0.50 | 20 |
| Nucleation Mode Characteristic Radius | 0.005 | 0.2 | 40 |
| Accumulation Mode Characteristic Radius | 0.05 | 2.00 | 40 |
| Coarse Mode Characteristic Radius | 0.50 | 4.50 | 41 |

* For the nucleation mode, there are 20 increments of optical depth, ranging from 0.025 to 0.50.

Table 2. MISR Climatology of Pure Particle Types*

| Aerosol Type | r_1 (μm) | r_2 (μm) | r_c (μm) | σ | α | nr | n_i (band) | ω_0 (0.67 μm) | Shape | RH (%) | Vary with RH? |
|--|----------------------------|----------------------------|----------------------------|----------|----------|------|--|-------------------------------------|--------------------------------------|-----------|---------------------|
| Sulfate 1 (Accum.) | 0.007 | 0.7 | 0.2 | 1.86 | n/a | 1.53 | 0.0 (all) | 1.0 | Spheres | 0 | yes |
| Sulfate 2 ^s (Accum.) | 0.05 | 2.0 | 0.45 | 1.30 | n/a | 1.43 | 0.0 (all) | 1.0 | Spheres | Amb | no |
| Mineral Dust [†] (Accum.) | 0.05 | 2.0 | 0.47 | 2.60 | n/a | 1.53 | 0.0085(1) 0.0055(2) 0.0045(3) 0.0012(4) | 0.91 | Prolate/ Oblate Spher- oids | 0 | no |
| Mineral Dust [†] (Coarse) | 0.5 | 15.0 | 1.90 | 2.60 | n/a | 1.53 | 0.0085(1) 0.0055(2) 0.0045(3) 0.0012(4) | 0.70 | Prolate/ Oblate Spher- oids | 0 | no |
| Sea Salt (Accum.) | 0.05 | 1.0 | 0.35 | 2.51 | n/a | 1.50 | 0.0 (all) | 1.0 | Spheres | 0 | yes |
| Sea Salt (Coarse) | 1.0 | 20.0 | 3.30 | 2.03 | n/a | 1.50 | 0.0 (all) | 1.0 | Spheres | 0 | yes |
| Soot | 0.001 | 0.5 | 0.012 | 2.00 | n/a | 1.75 | 0.455(1) 0.440(2) 0.435(3) 0.430(4) | 0.17 | Spheres | 0 | no |
| Biomass Burning ^{††} | 0.007 | 2.0 | 0.13 | 1.80 | n/a | 1.43 | 0.0035 (all) | 0.98 | Spheres | 97 | no |
| Near- surface Fog [‡] | 0.5 | 50.0 | n/a | n/a | 2.5 | 1.33 | 0.0 (all) | 1.0 | Spheres | 100 | no |
| Thin Cirrus ^{††} | 10.0 | 500. | n/a | n/a | n/a | 1.31 | 0.0 (all) | 1.0 | Fractal | 100 | no |

*In this table, r_1 and r_2 are the lower and upper radius limits for the particle size distribution. Particle types having r_c and σ specified are distributed log-normally, with characteristic radius r_c and width σ ; those having α specified are power-law distributions with exponent α . ω_0 is the single scattering albedo, given here at the effective wavelength of the MISR red channel. RH is the relative humidity for which the particle size distribution and indices of refraction are listed. The last column indicates that the properties of Sulfate 1 and Sea Salt particles are assumed to vary with relative humidity, using the hydration model of Hanel (1976). The aerosol physical data are abstracted from Shettle and Fenn (1979), d'Almeida et al. (1991), WCP (1984), and other sources, except as indicated. Optical data for spherical particles are calculated using Mie theory.

^s Stratospheric aerosol model based on Wang et al., 1989.

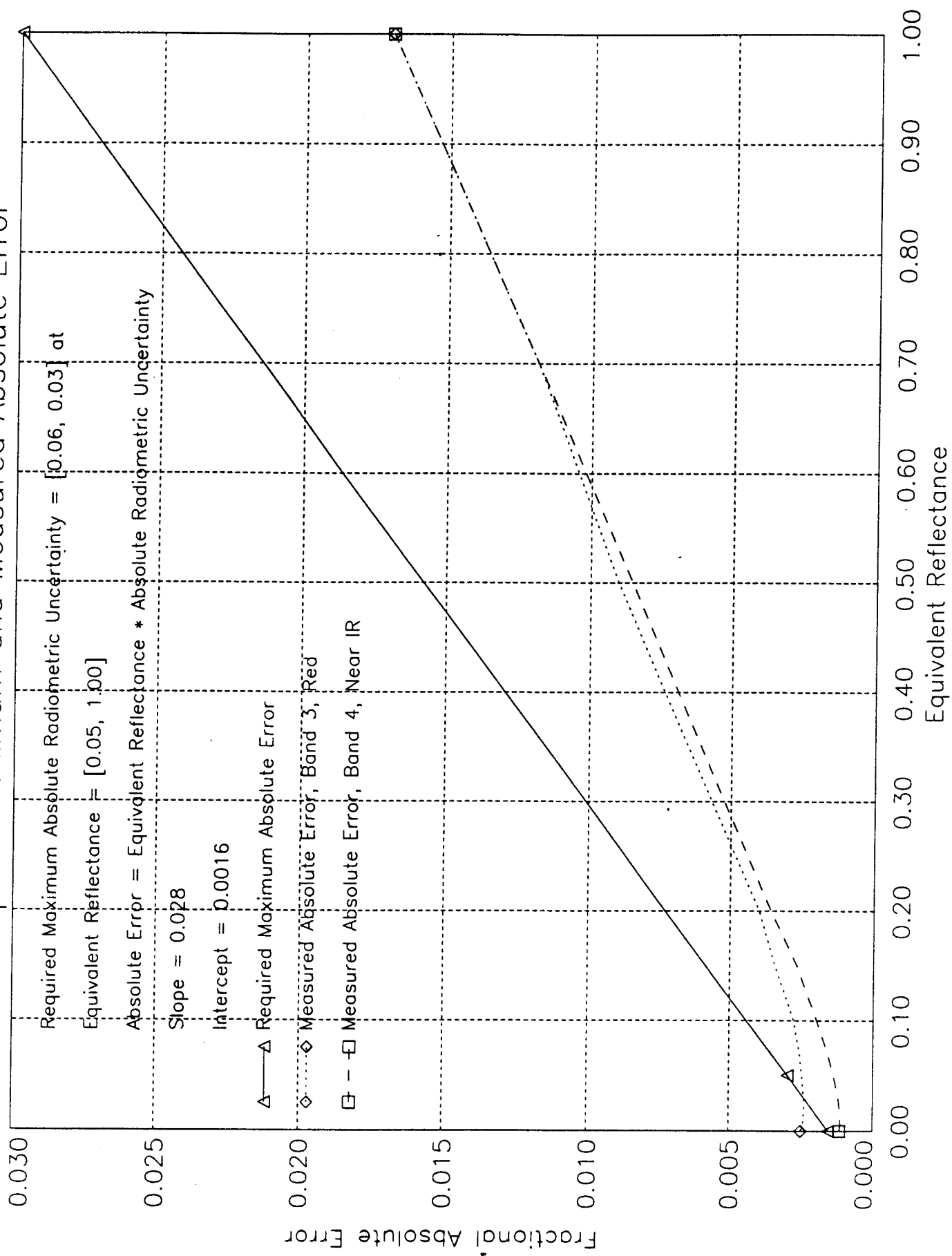
[†] Non-spherical mineral dust models based on Mishchenko et al., 1997.

^{††} Biomass burning particle model based on Remer et al., 1997.

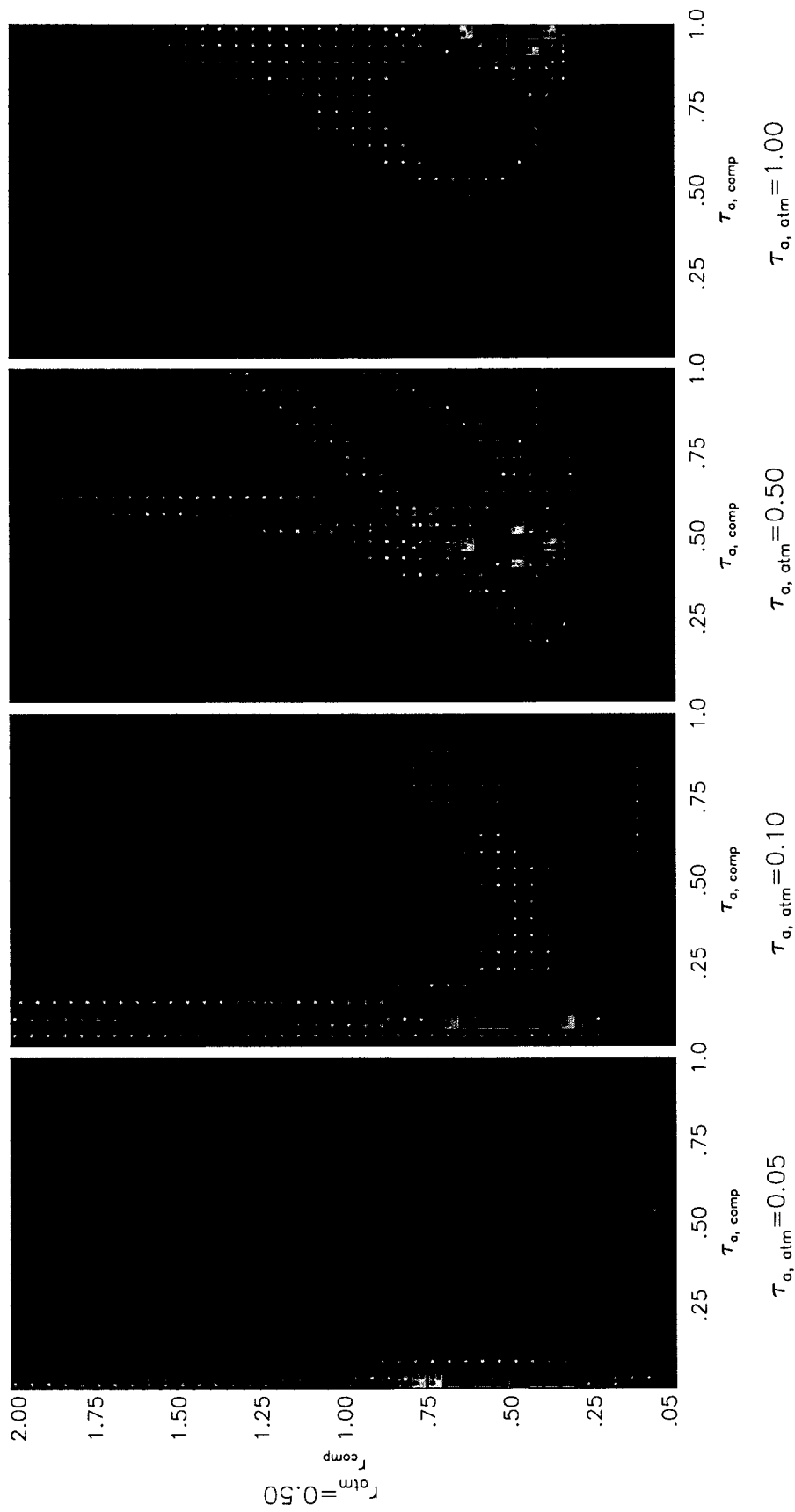
[‡] Near-surface fog model based on Prupacker and Klett, 1978.

^{††} Fractal thin cirrus model based on Mishchenko et al., 1996.

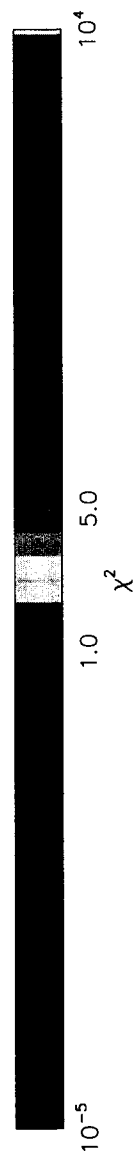
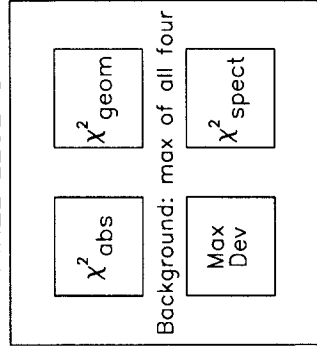
Required Maximum and Measured Absolute Error

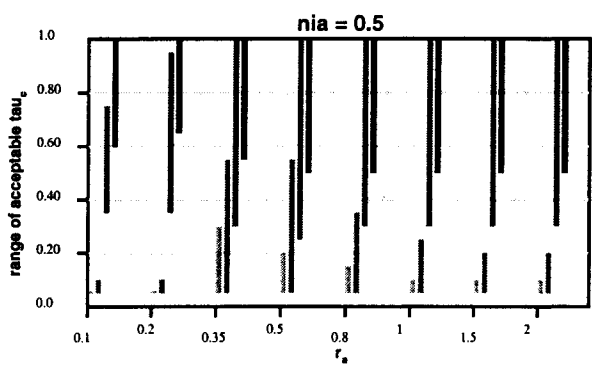
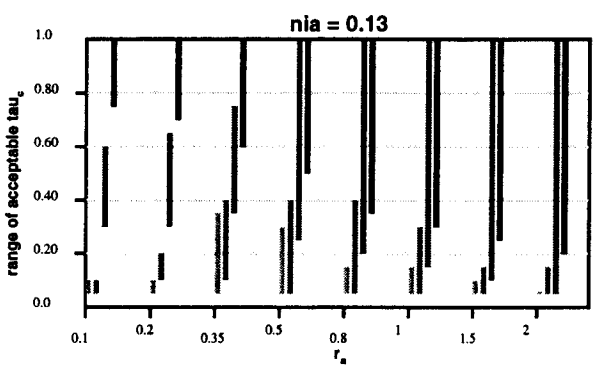
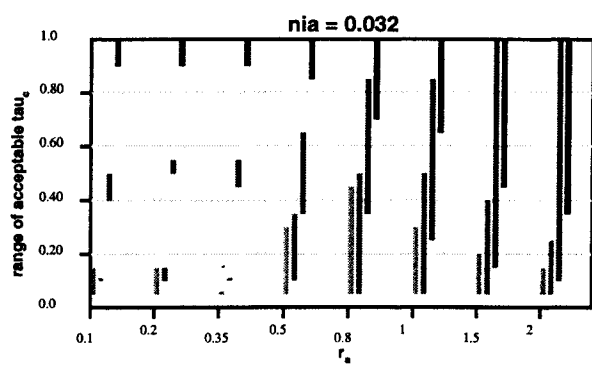
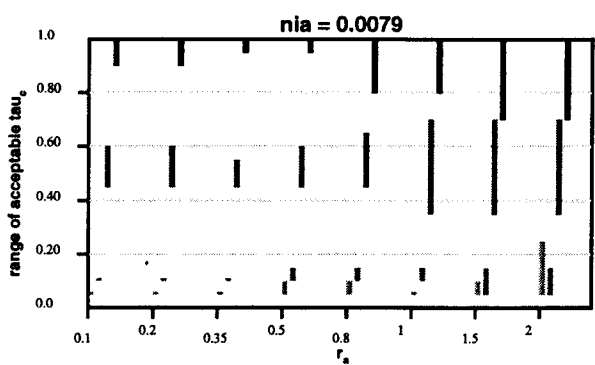
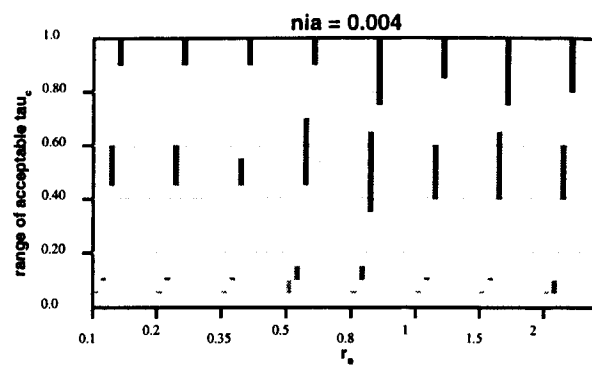
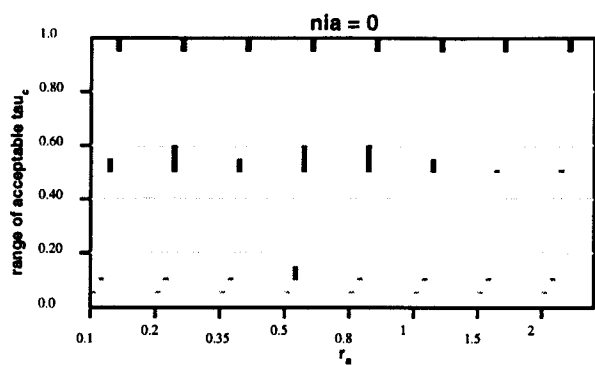


N_r 1.53 N_i 0.0 Atmosphere and Comparison (Fresnel Surface)
 $RH_{atm} = 0.70$ $RH_{comp} = 0.70$ $\mu_o = 0.60$ $\Delta\phi = 26.0$



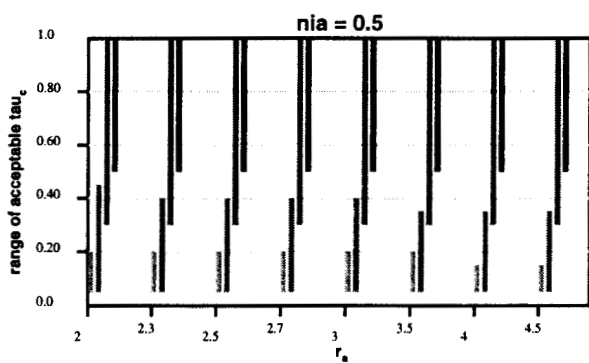
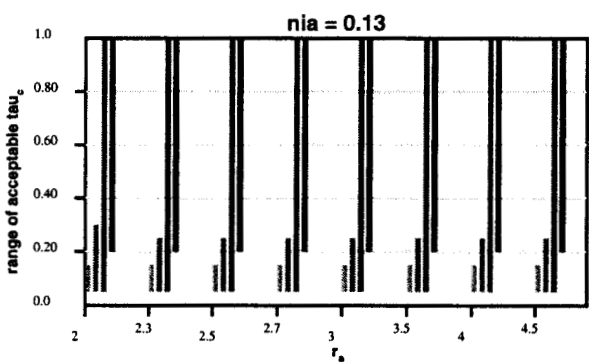
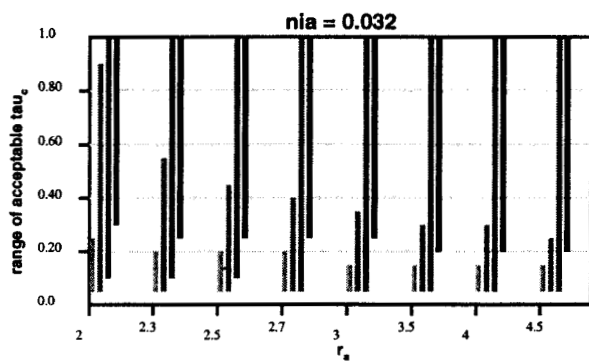
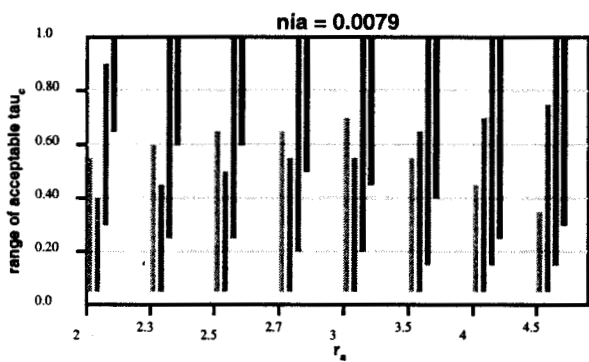
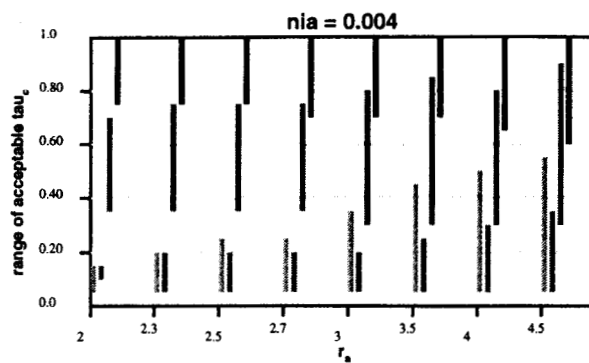
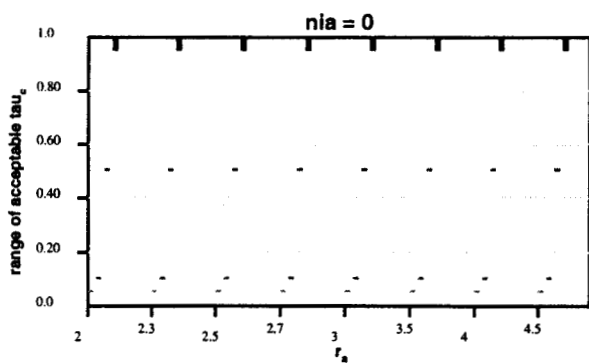
PIXEL LEGEND





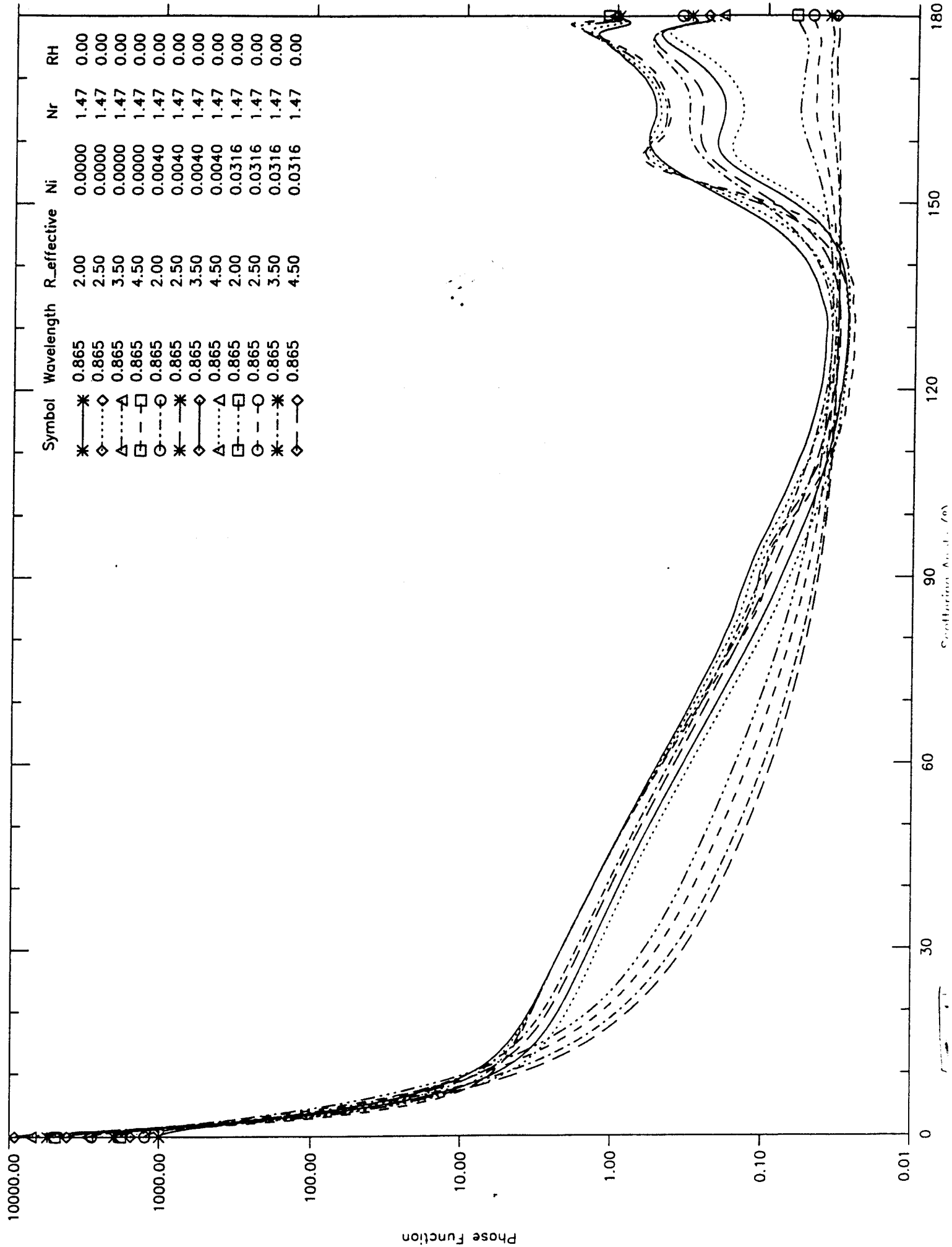
\approx accump

Fig 3 A



τ_{coarse}

Fig 38



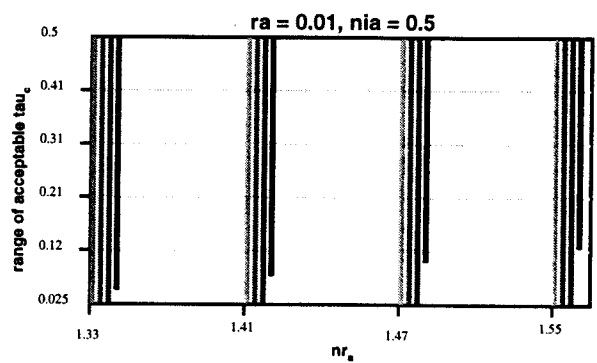
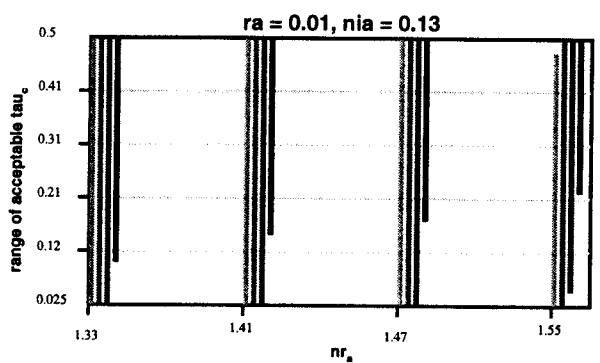
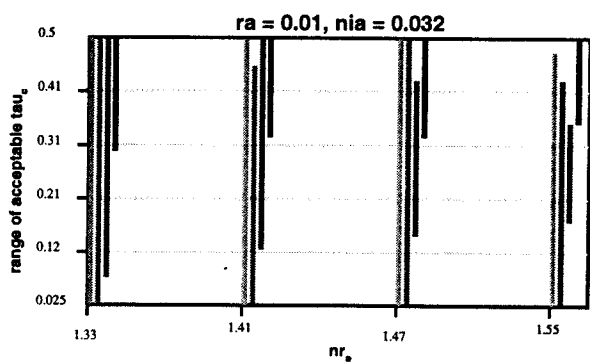
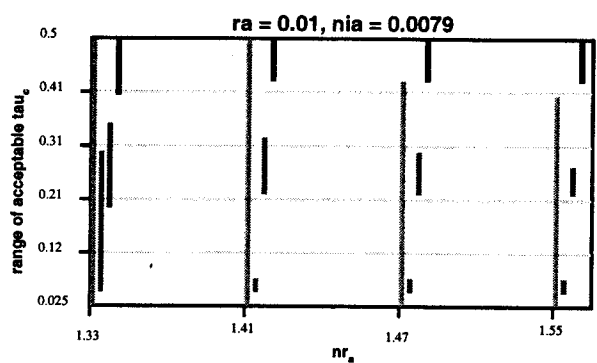
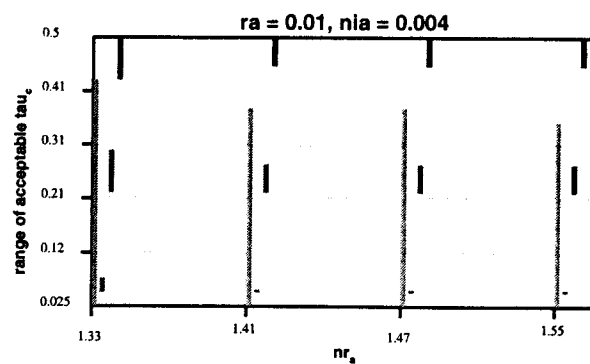
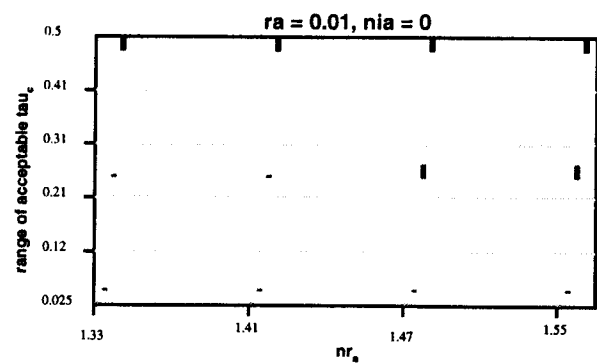


Fig 5

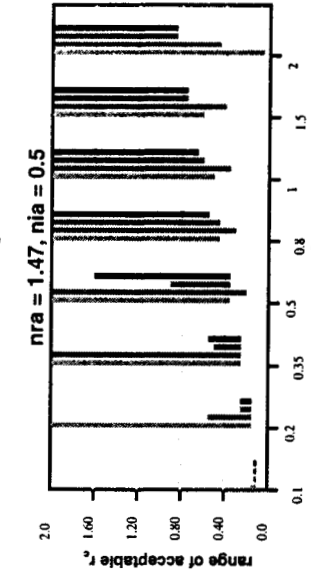
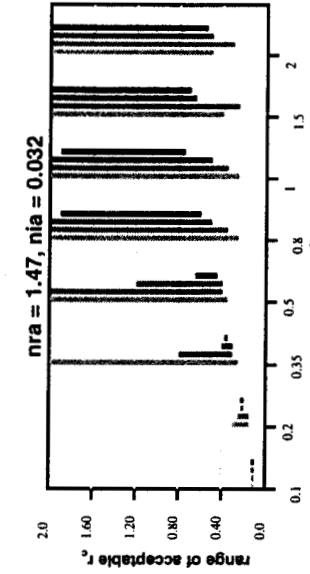
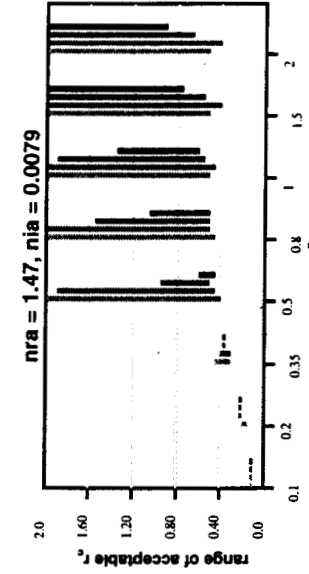
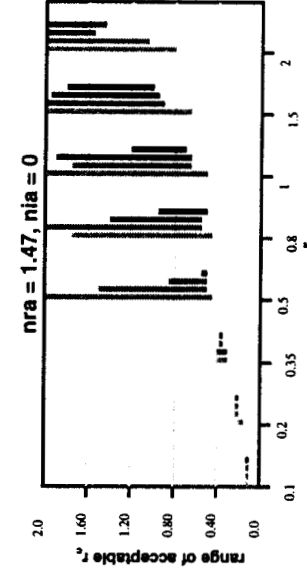
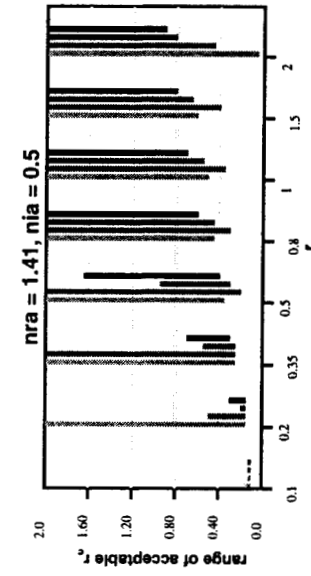
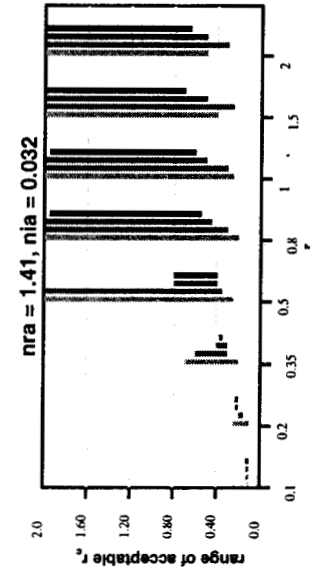
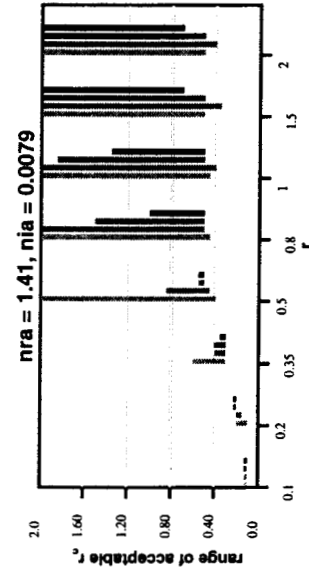
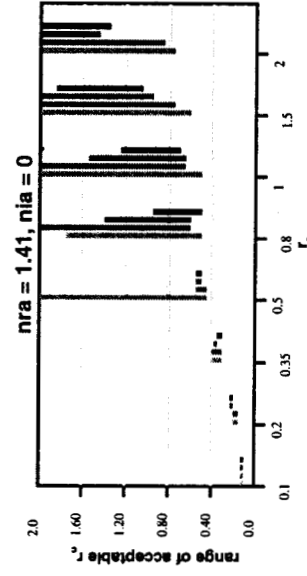
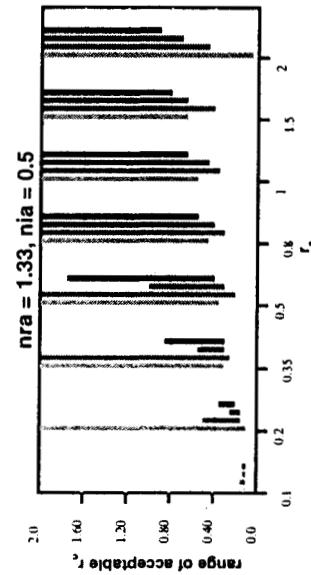
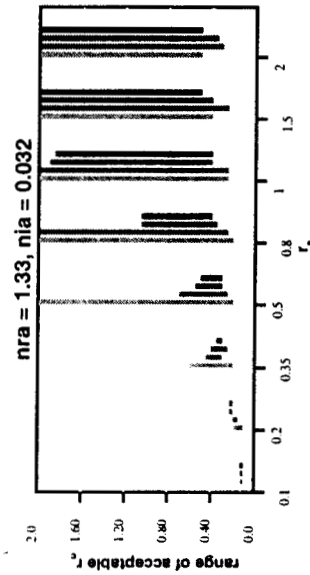
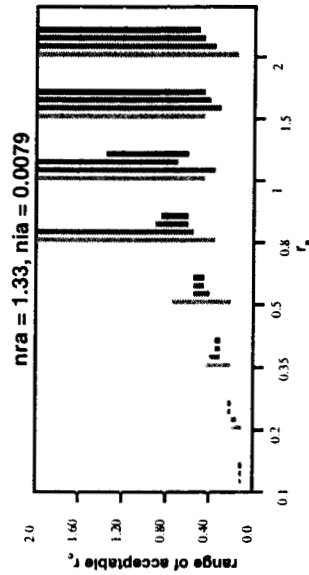
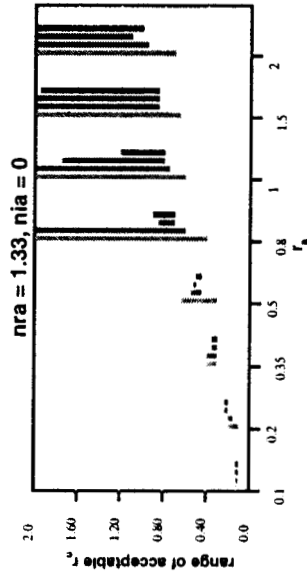
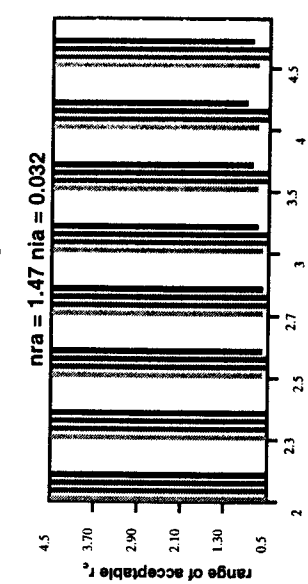
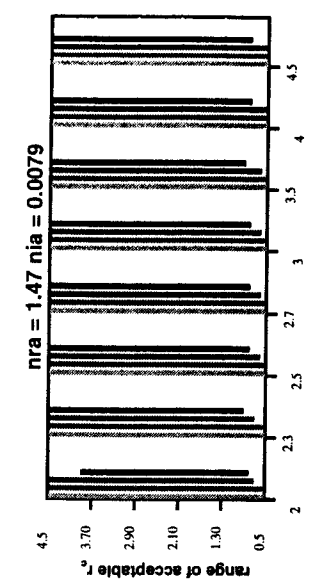
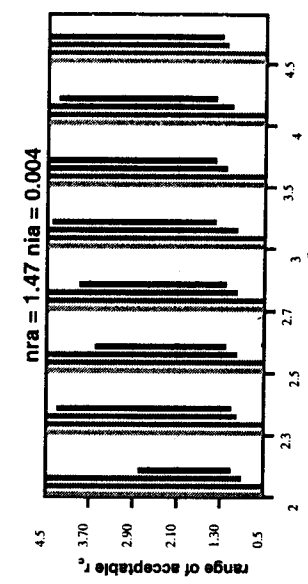
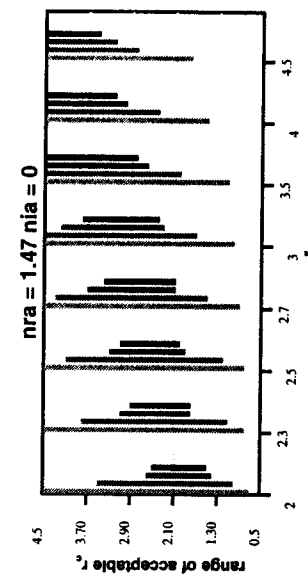
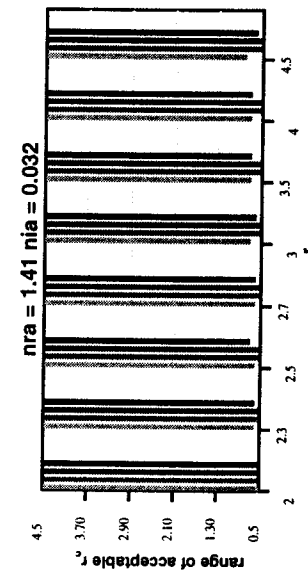
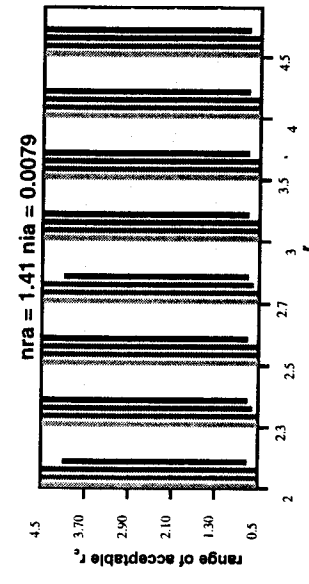
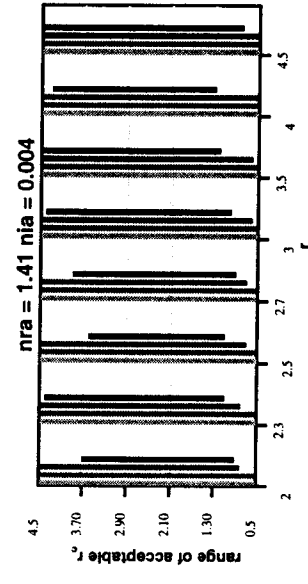
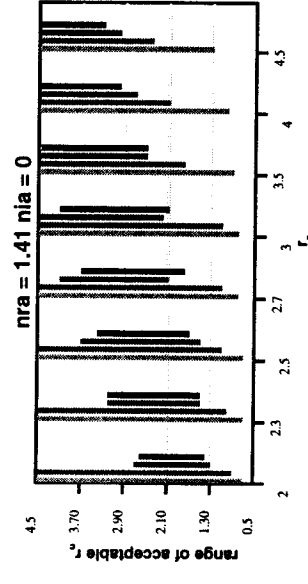
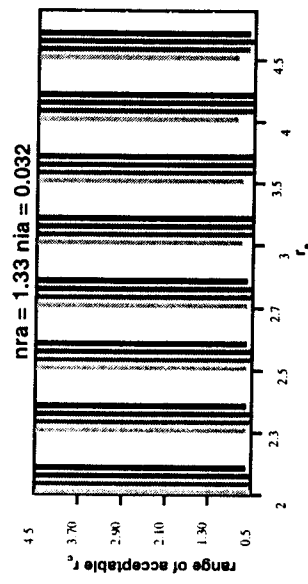
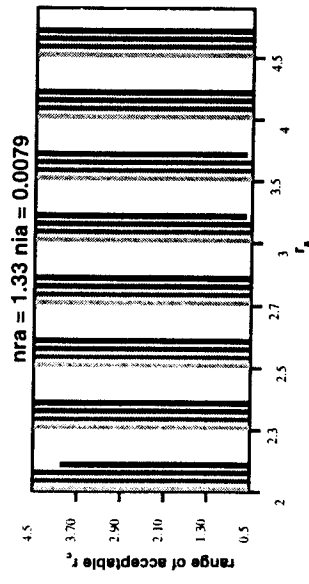
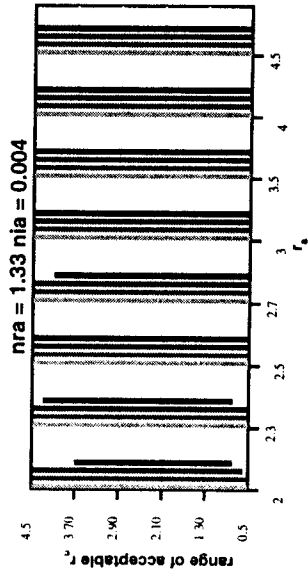
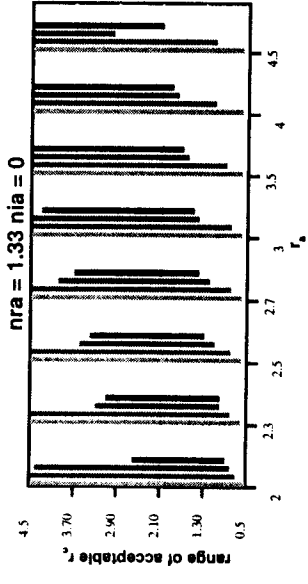


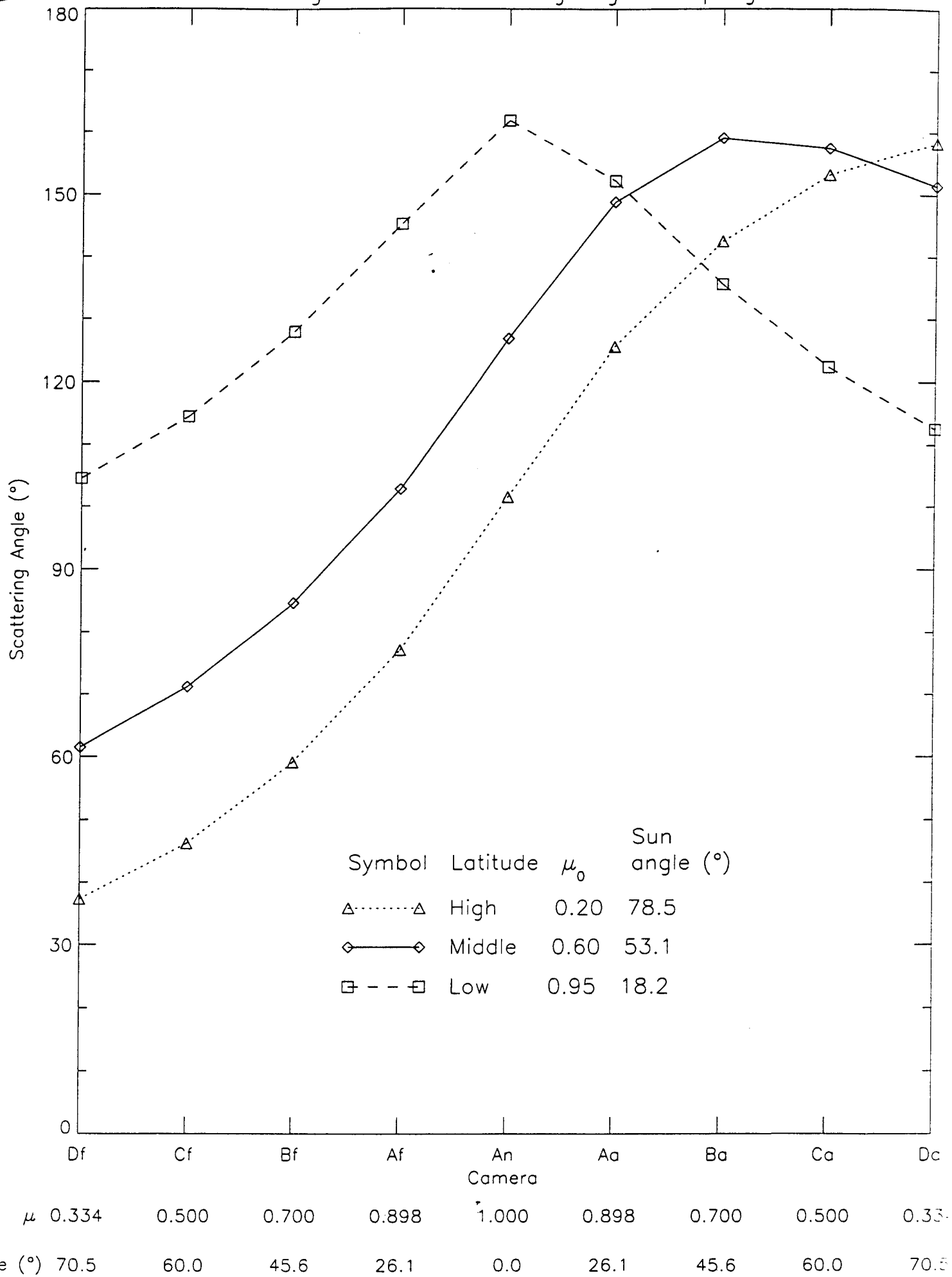
FIG. 6A

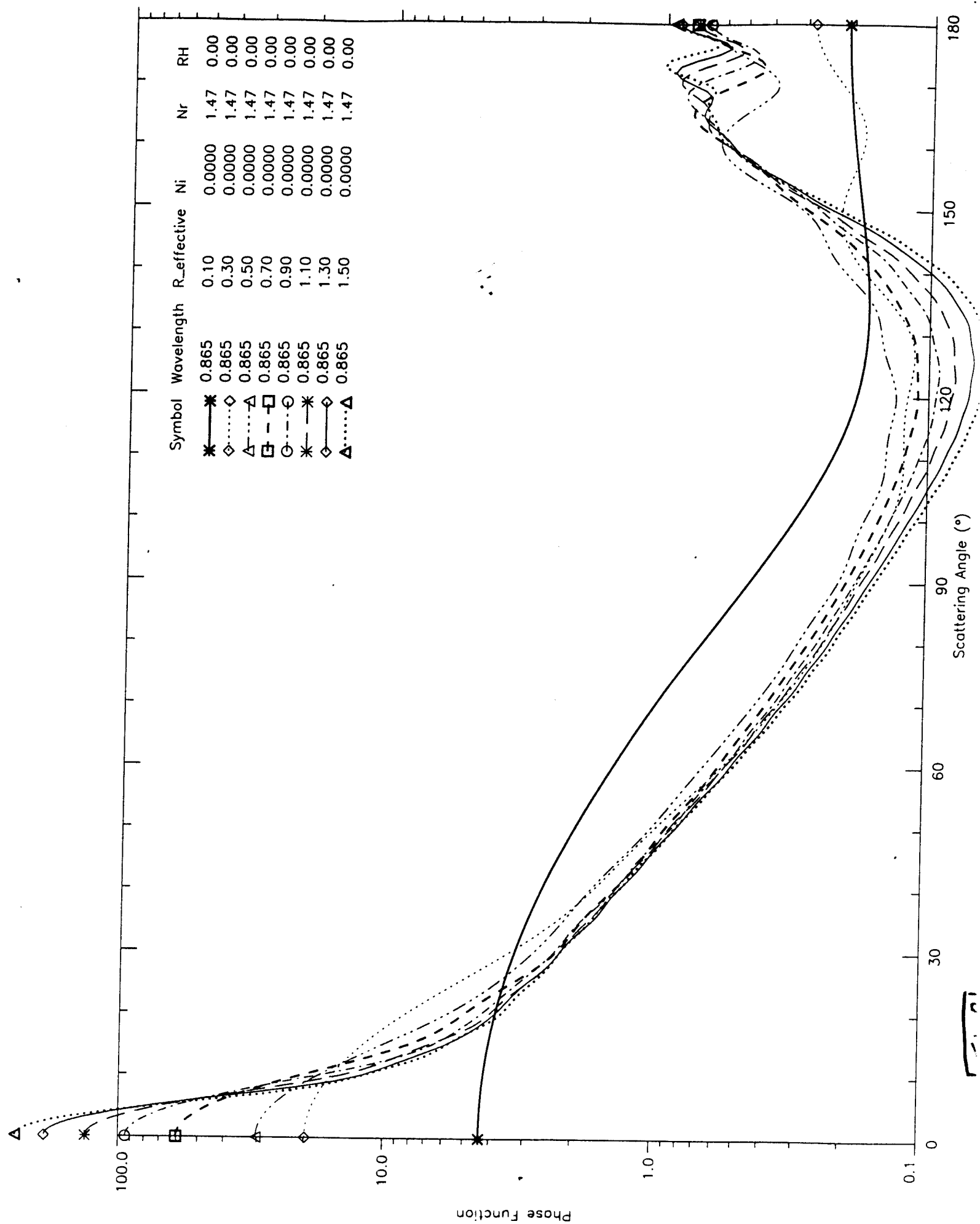


1.47, 68

F₇

Range of MISR Scattering Angle Sampling





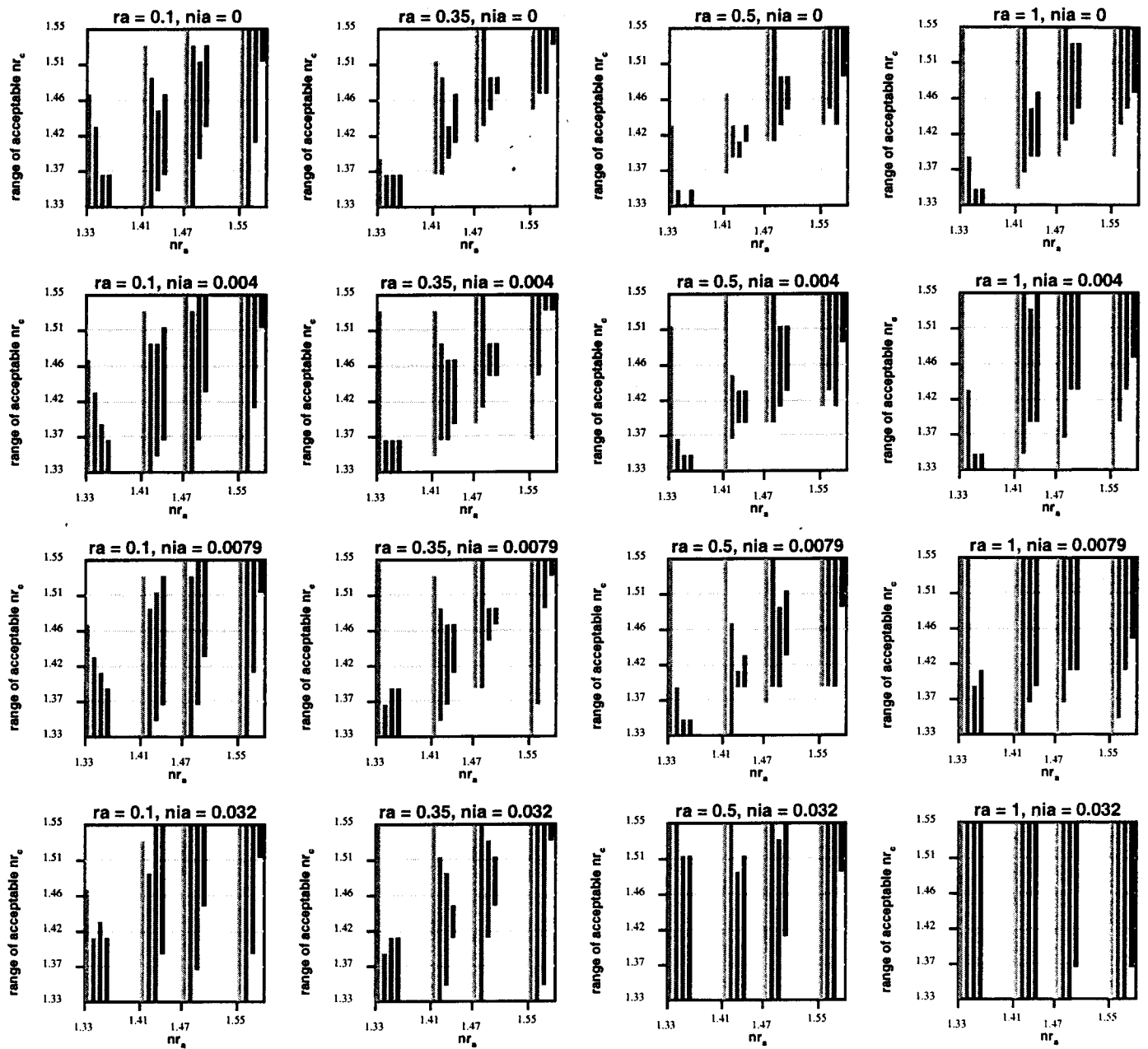
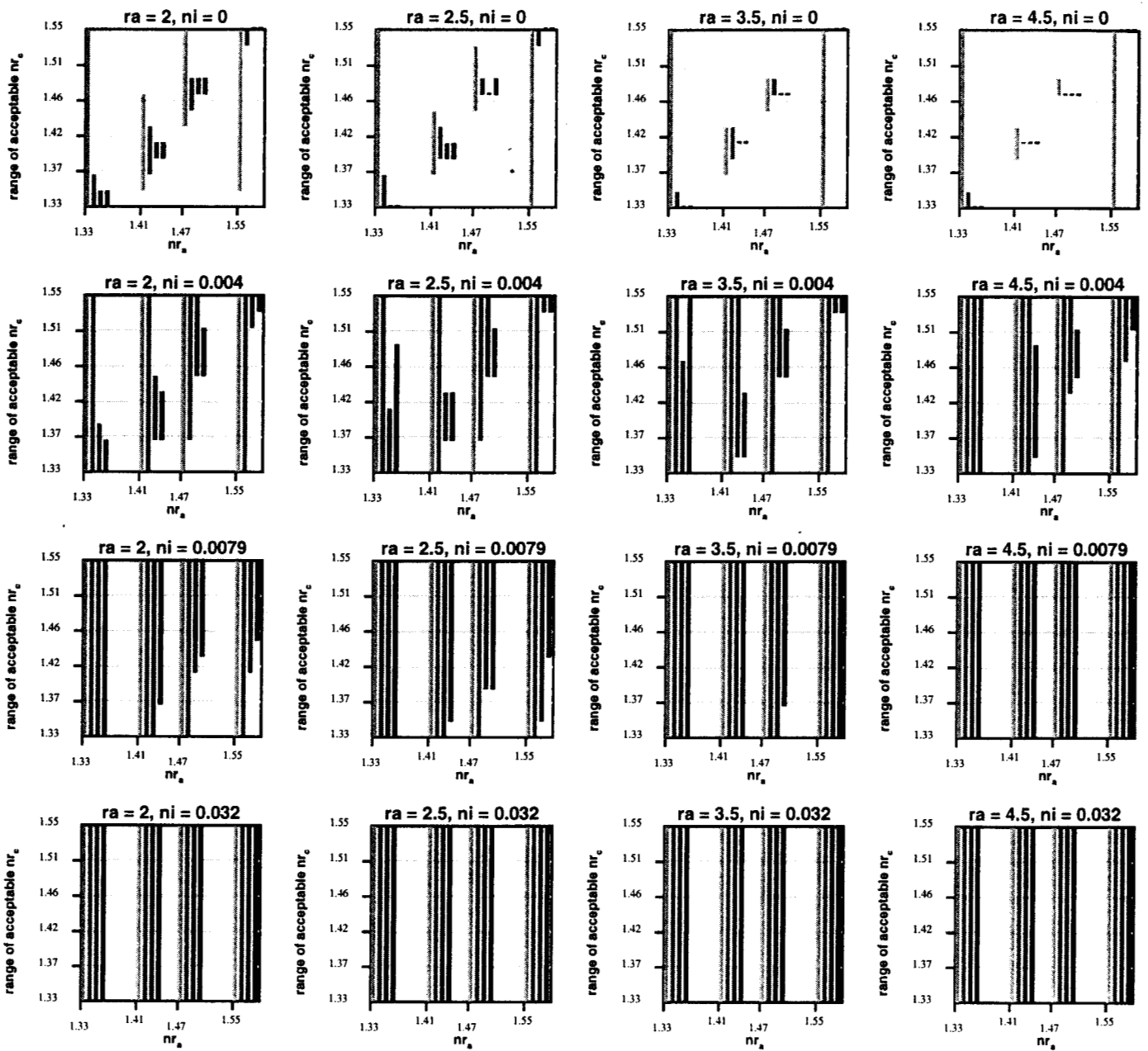
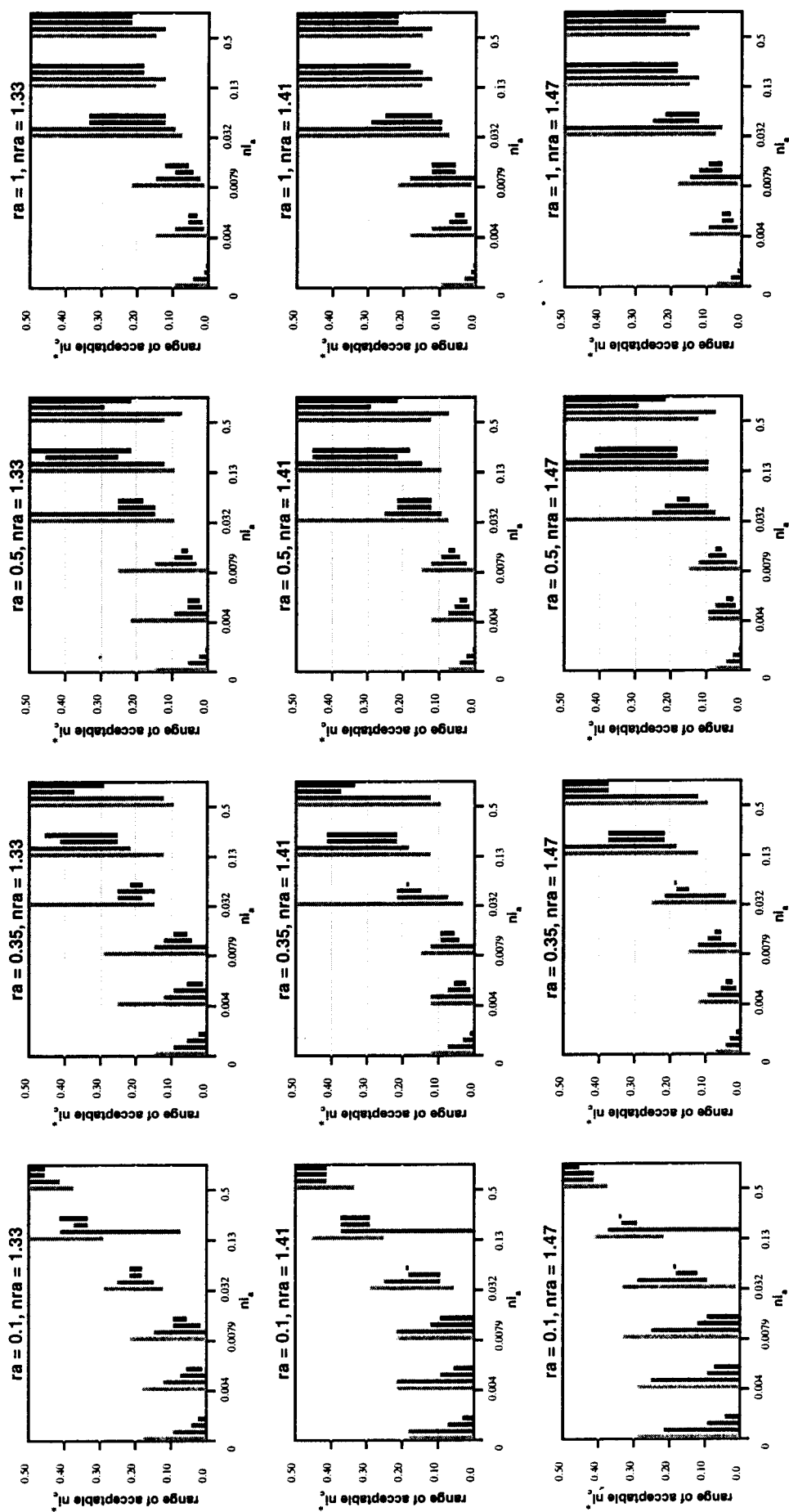


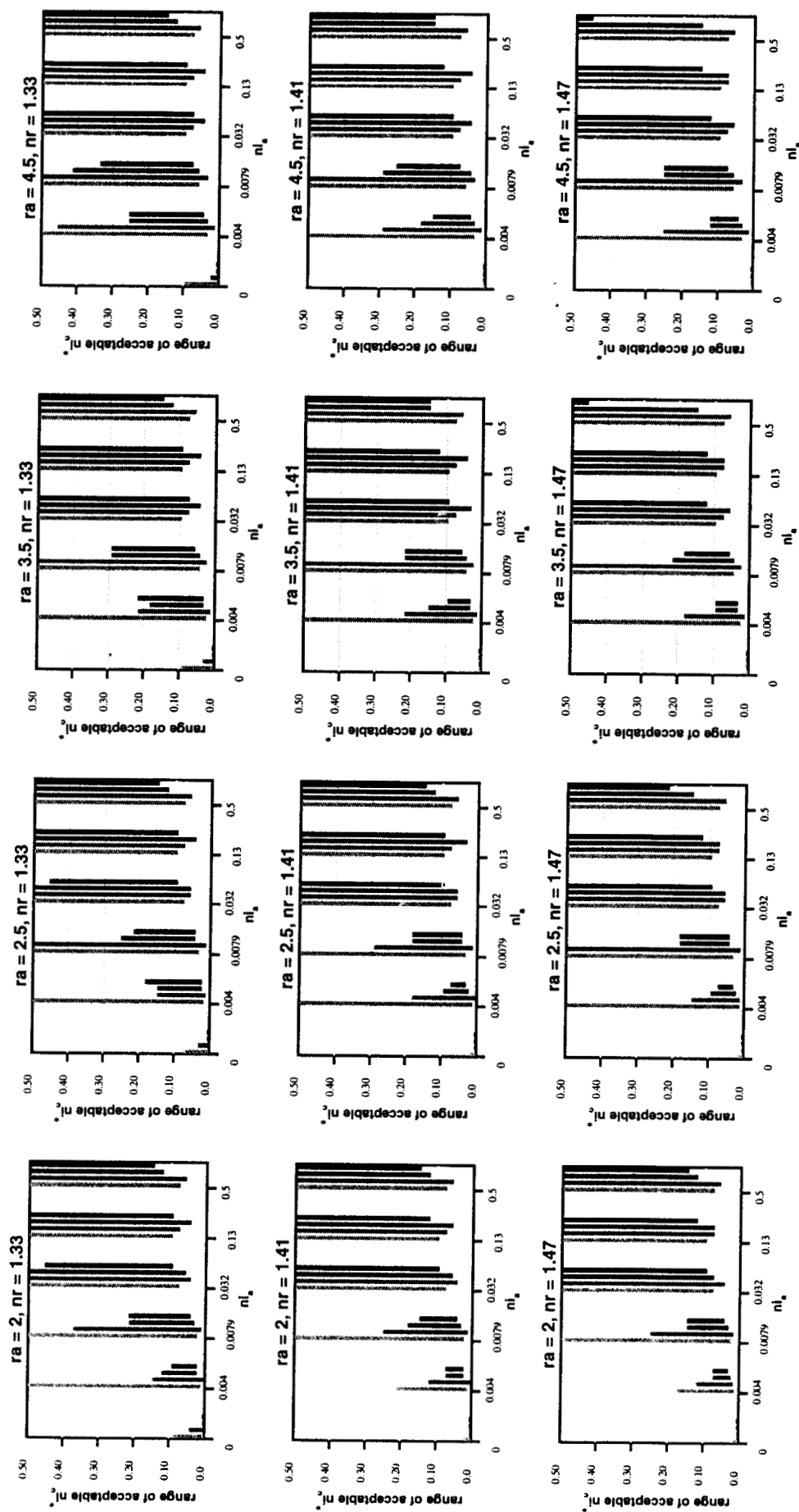
FIG. 9A





* The vertical axis has been scaled as $\log_{10}(1.0 + 100.0 * (\text{range of acceptable } n_i^*))$

FIG. 10A



* The vertical axis has been scaled as $\log_{10}(1.0 + 100.0 * (\text{range of acceptable } n_i^*))$